

# Micro-Optics

---

Design of an optical tweezers using the evanescent field from microtapered fibres

Laura Russell, 104375696



# 1. CONTENTS

1.	<b>Contents</b> .....	1
2.	<b>Abstract</b> .....	2
3.	<b>Introduction</b> .....	3
4	<b>Section 1 - Instrumentation</b>	
4.1	Background Theory .....	4
4.2	Experimental Design.....	7
4.3	Results & Discussion .....	9
5	<b>Section 2 - Optical Tweezers</b>	
5.1	Background Theory .....	16
5.2	Experimental Procedure .....	26
5.3	Results & Discussion .....	30
5.4	Conclusion.....	40
6.	<b>Acknowledgements</b> .....	41
7.	<b>References</b> .....	42
8.	<b>Appendix A – Specification Sheet</b> .....	44

## 2. ABSTRACT

This undergraduate project focuses on the evanescent fields generated from microtapered fibres and their use in *optical trapping* experiments – applications of which are prevalent in biophysics and cold atom manipulation techniques. The theoretical background on which optical trapping is based is first described and an outline of the experiment follows. Several skills associated with optical fibre manipulation and general electronics are gained throughout the project. Fabrication of micron tapered tapers is mastered utilising a computerised heat and pull rig. With the use of a fibre-coupled 140mW CW diode laser source, observations contrary to those seen in literature are made – an apparent anti-trapping effect is evident. Extensive use of imaging software and analysis is used to investigate the behaviour of the polyamide seeding particles under this anti-trapping force. Section 1 concentrates on general instrumentation and a short study of quantum dots, while section 2 contains the investigation of optical trapping. The conclusion highlights some improvements which can easily be made to the experiment.

### 3. INTRODUCTION

Since the first demonstration of optical tweezers in 1986<sup>[1]</sup>, the advantages of this particle-manipulation technique have revealed themselves in many scientific research areas. For example, we now have protein unfolding with micro traps and comprehension of the mechanism by which bacterium propel themselves in the body from optical tweezers experiments.<sup>[2]</sup> While the experimental designs of the optical tweezers have not changed drastically, the refinement of the traps have increased to allow control over objects from the micron scale right down to single atoms. Optical tweezers can be used to propel doped glass microspheres and polystyrene beads – further, microspheres demonstrate lasing under whispering gallery mode resonance and are of interest to optical networks.<sup>[3][4]</sup> In the quantum technology domain, quantum system control is ever more reliant on cold atom methods – an area which is strongly reliant on laser manipulation of atomic particles.

In 2007, it was shown that optical trapping could be successfully achieved using the evanescent field from a submicron tapered optical fibre (Brambilla, Murugan, Wilkinson, & Richardson, 2007). This experiment utilised a 500mW CW laser source and found that polystyrene beads could be trapped and propelled at speeds  $\sim 10\mu\text{m/s}$  with the evanescent field.<sup>[5]</sup> This project investigates the lower limit of laser power to achieve trapping: how much power do we actually need to trap micron particles?

In future applications, enhancement of the evanescent waves (with, for example, gold sputtering techniques) from these tapers can be explored to achieve trapping with even lower laser power. With a looser requirement for optical field strength, the path ahead is paved for inexpensive optical tweezers in biophysics and photonics.

## 4. SECTION 1 – INSTRUMENTATION

The first three weeks of the project provided an introduction to the wide range of techniques used in the field of quantum optics. The use of lasers for spectroscopy, point-and-accumulate spectrometers and optical fibre handling are essential for research in *atom optics*. Atom optics is concerned with wave characteristics such as diffraction, interference and reflection on an atomic level. Further, the optical trap as already introduced is, fundamentally, localization of atoms in small volumes. These topics encourage experimental probing of micro structures such as *quantum dots*.

### 4.1 BACKGROUND THEORY

#### 4.1.1 Light Amplification by Stimulated Emission of Radiation – The Laser

The laser achieves light amplification by taking advantage of energetic atoms in a medium to enhance the light field. Einstein, in 1916, formulated the idea of dynamic equilibrium which exists for an object which is radiated by electromagnetic waves. When photons are ‘pumped’ into an *active medium*, they impart their energy to atoms which contain energy levels separated by energies equal to that of the incident photon. The atoms jump to higher energy levels and remain there for timescales of ~10 ns before re-emitting the absorbed energy as a photon and returning to a stable state.<sup>[6]</sup> This process is called *spontaneous emission*. In a dense medium, this re-emitted energy can be absorbed by neighbouring atoms. A variation on the process of spontaneous emission is *stimulated emission*. Stimulated emission occurs when a photon is absorbed and re-emitted by an already-energetic atom. The result is that two photons are emitted from the single atom which has returned to its stable state. The emitted photons are not only in phase, they also have the same polarizations and propagation directions.

In a laser, we aim to have the majority of the atoms in excited energy states – a population inversion according to the Maxwell-Boltzmann distribution. This would allow an incident photon, with appropriate frequency, to trigger an avalanche of in-phase photons to be emitted during the stimulated emission process. Provided there is no dominant scattering processes within the media and that this population inversion could be maintained, a highly coherent beam of light can be generated from the active medium.

There are many types of laser using various configurations of active media to generate lasing. A gas laser, for example, is one which generates light by discharging an electric current through a gas. In 1960, Ali Javan, William Bennett Jr. and Donald Herriott achieved CW emission of the first helium-neon gas laser (Javan, Bennett Jr., & Herriott, 1961).<sup>[7]</sup> In Section 2, the *semiconductor diode laser* is explored in greater detail as it was fundamental to the optical trapping experiment.

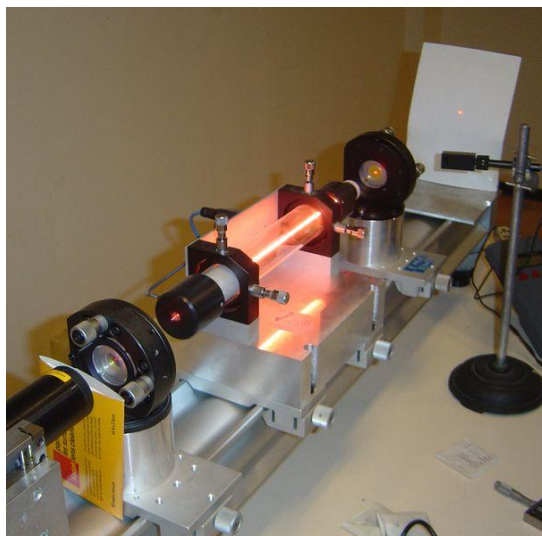


Figure 1: A HeNe gas laser showing electrical discharge in a gas chamber. Copyright © 2004 David Monniaux.

### 4.1.2 Quantum Dots

A quantum dot is a semiconductor structure which exhibits confinement of electron-hole pairs (*excitons*) in three dimensions. Similarly, exciton confinement in just one and two dimensions of a semiconductor describe a quantum well and quantum wire, respectively. The quantum dot system, under confinement, becomes quantized according to the energy levels given by –

$$E_{i,j,k} = \frac{h^2}{8m^*} \left( \frac{i^2}{L_z^2} + \frac{j^2}{L_y^2} + \frac{k^2}{L_x^2} \right)$$

$L_z$ ,  $L_y$ , and  $L_x$  are the confining dimensions, the indices (ijk)=(123) are the quantum confinement numbers, and  $m^*$  is the effective carrier mass\*. We assume the zero-point of energy is at the confined layer conduction band edge.<sup>[8]</sup>

One of the most interesting properties of quantum dots is that their optical behaviour depends on their size. For instance, in UV light a 2.3 nm *cadmium selenide* dot glows turquoise, whereas a 5.5nm dot of the same material glows orange. This is because the three-dimensional confinement causes the band gap energy to vary with the dot's size. Larger quantum dots have more densely-packed energy levels and thus it can absorb and emit lower energy (red) photons. The opposite is true of smaller quantum dots – the energy gaps are less densely-packed and so the dot will absorb and emit higher energy photons (“blue” photons). Figure 2 shows a colourful array of quantum dots in a liquid solvent.

---

\* The effective mass is a correction which arises because, in most cases, electrons and holes in crystals respond to the **E** and **H** fields as if they were free particles in a vacuum, but with differing masses.

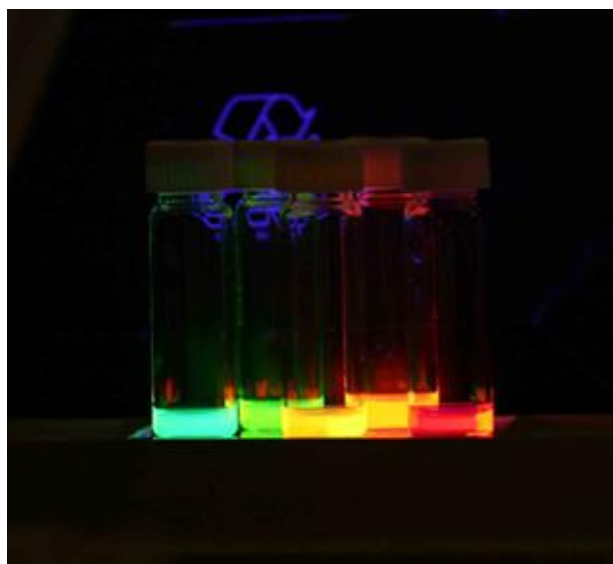


Figure 2: A rainbow of quantum dots. Each vial contains a mono-disperse sample of quantum dots in a liquid solvent. Copyright © Walkman16.

### 4.1.3 Spectroscopy

Spectroscopy is the study of light-matter interaction with respect to wavelength,  $\lambda$ , frequency,  $\nu$ , or energy,  $E$ , as given by Planck's  $E=h\nu$ . A spectrometer is an instrument which is used to measure various properties of an electromagnetic wave such as intensity or polarization – in particular, if we have a strongly coherent light source such as a laser, we can obtain very narrow spectral lines and thus identify, very precisely, the associated wavelength.

The spectrometer used in this project (see Appendix A for specifications) utilised an array of CCD's – a line of light-sensitive diodes which convert photons to electrons. The more intense the incident light on the spectrometer is, the greater the electrical charge which accumulates on the diode. When coupled with computer software, intensity versus wavelength spectra can be obtained.

The use of a spectrometer in this project allowed the absorption and emission characteristics of quantum dot samples to be investigated. By 'pumping' the samples with various light sources, we obtain spectra with peaks due to emission and troughs due to absorption.

## 4.2 EXPERIMENTAL DESIGN

Two classes of laser were used in the following investigations. A summary of their primary properties is displayed below.

<i>Laser</i>	<i>HeNe</i>	<i>Diode</i>
<i>Class</i>	3b	2
<i>Wavelength</i>	633 nm	~533 nm
<i>Max CW Power</i>	3 mW	1 mW

### 4.2.1 Laser Spectra

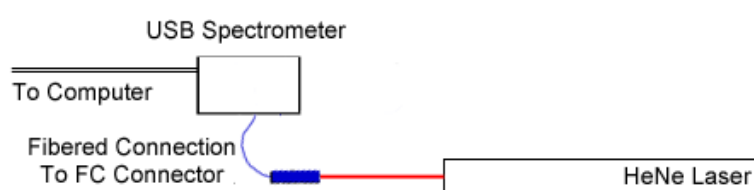


Figure 3: Apparatus used to examine the spectrum from a laser.

Using an optical breadboard, a 633 nm HeNe gas laser was mounted on stands and positioned so that the beam was coupled into a USB spectrometer (see *Figure 3* above). The USB spectrometer was connected to a computer with *OOIBase32* software. An FC fibre connector was used to connect a fibre optic cable to the spectrometer unit. When the HeNe laser was powered on, a spectrum was viewed on screen. A text file of this spectrum was exported for analysis in *Origin 8.0* and screenshots were taken. The same procedure was followed for the diode laser and an ambient light spectrum was taken by switching off any nearby laser sources and viewing the resulting signal on screen.

### 4.2.2 Quantum Dot Spectra

The experimental apparatus was set up as shown in **Error! Reference source not found.** below. Using an optical breadboard, a 633 nm HeNe gas laser was mounted so that it pointed at the first sample of quantum dots. A USB spectrometer was mounted in a position which minimized HeNe laser light accumulation and maximised emissions from the quantum dots. A 0.5 density filter was placed between the laser and sample to reduce saturation of the desired quantum dot spectrum by a factor of  $10^{-0.5}$ . The laser was powered on and the resulting spectrum from the quantum dot sample was viewed on screen with *OOIBase32*. This spectrum was exported as a text file and screenshots were taken.

The same procedure was followed using the diode laser, a table lamp (in each case without the 0.5 density filter), and with ambient light. Then, this was repeated once again for the second sample of quantum dots.

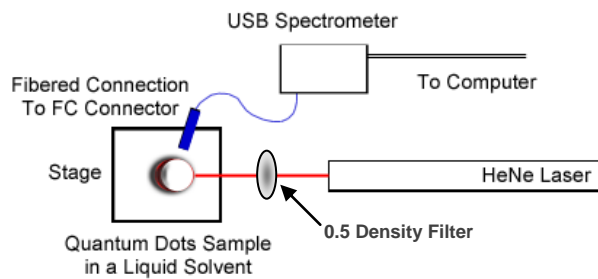
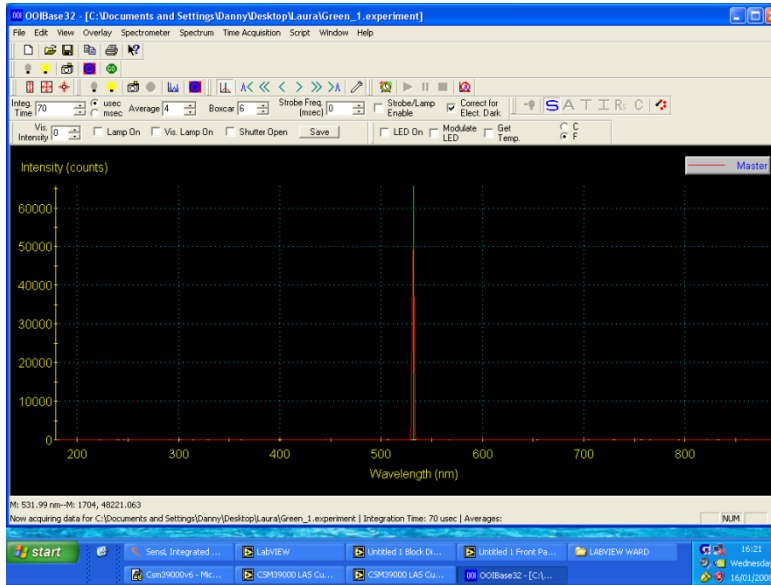


Figure 4: Apparatus used to examine the spectrum from an emitting sample of quantum dots.

### 4.3 RESULTS & DISCUSSION

#### 4.3.1 Laser Spectra

The laser spectra obtained initially with OOIBase32 were exported as text files and plotted in Origin 8.0. The resulting plots are displayed below in Figs. 5 – 7. The expected wavelength peak value for the diode laser was 533 nm and the observed 532.79 nm. This discrepancy is due to the temperature-dependent nature of the diode laser.



Wavelength nm	Intensity Wm <sup>-2</sup>
529.42	31.382
529.62	34.451
529.82	33.382
530.02	59.451
530.21	54.382
530.41	163.451
530.61	777.382
530.81	6512.452
531	25420.381
531.2	44360.453
531.4	47904.383
531.6	53349.453
531.79	59107.383
531.99	48364.453
532.19	35608.383
532.38	19428.451
532.58	10246.382
532.78	5803.452
532.98	3275.382

Figure 6: Exported data file from OOIBase32.

Figure 5: OOIBase32 software with green emission peak.

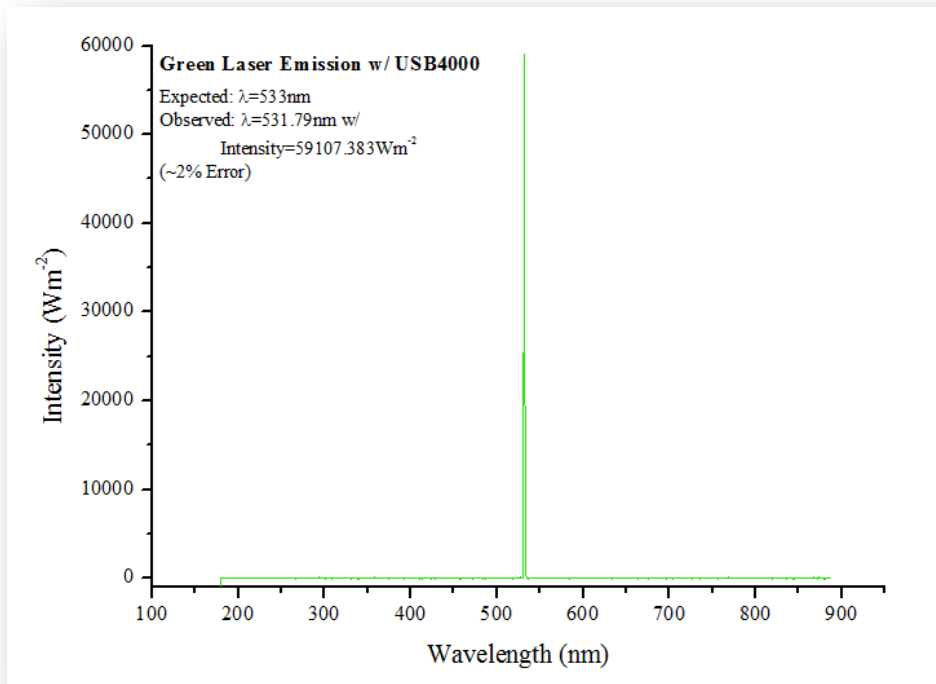
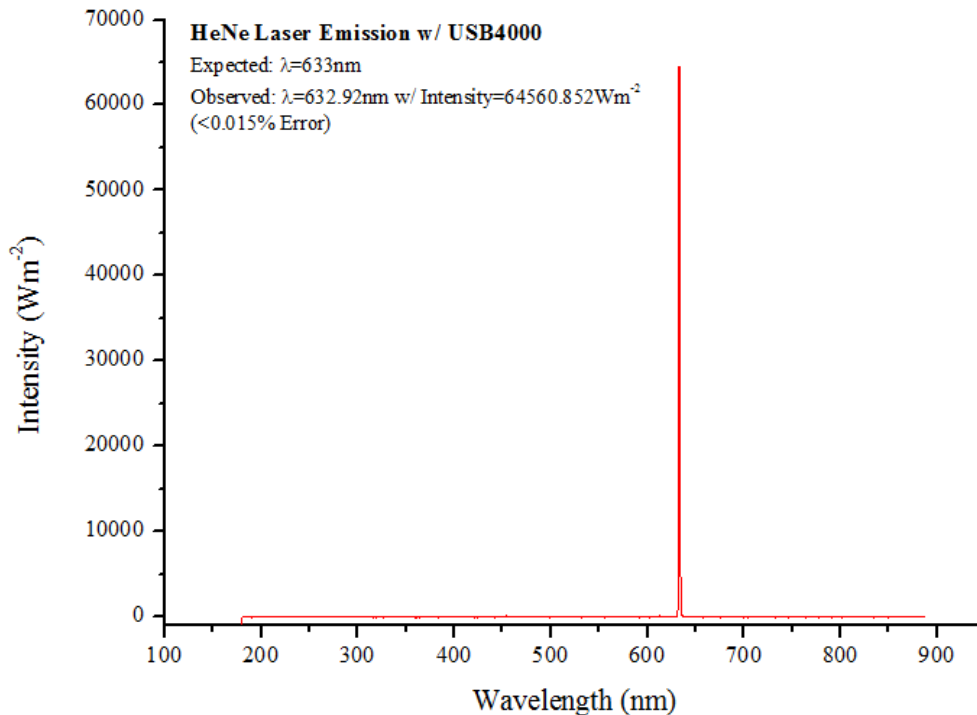


Figure 7: Final green diode laser spectrum.

Similarly, the observed HeNe laser spectrum is given below in *Figure 8*.



**Figure 8: The observed HeNe spectrum with a strong emission peak at ~633 nm.**

The expected wavelength is 633 nm and the observed is 632.92 nm. This indicates a  $< 0.015\%$  error – clearly negligible and accounted for by the USB4000’s precision.

### 4.3.2 Quantum Dot Spectra

A table summarizing the expected peak emission and absorption properties of the quantum dots is given below.

<i>Sample #</i>	<i>1</i>	<i>2</i>
<i>Absorption Wavelength [nm]</i>	591	554
<i>Emission Wavelength [nm]</i>	610	585

The following spectra (Figures 9 – 17) show broad emission bands around the expected emission wavelengths. In the case where the HeNe laser was used, saturation of the spectrum was observed at 633 nm which encouraged the use of a density filter. Sample 1, for the HeNe laser, then showed a strong emission around 640 nm interrupted by the characteristic red peak at  $\approx 633$  nm. A small absorption peak was observed at  $\approx 590$  nm – corresponding to the expected value of 591 nm. Sample 2 is much less telling until we examine closely the region around the base of the 633 nm peak. We do see a small absorption dip at approximately 554 nm – corresponding well with the expected value given above. The 629 nm emission is unusual but we see a large peak at 630 nm from the table

lamp source spectrum. There is a very slight rise in intensity in the 585 nm to 590 nm range which can be accounted for by the (expected) increased emission at 585 nm.

For both sample 1 and 2, the table lamp gives us a broad emission range once again – because of the broad frequency range of source light, we get some interesting peaks at 638 nm, 684 nm, 761 nm (sample 1) and 583 nm, 630 nm (sample 2). The ambient light gives us an even broader emission range suffering from noise due to the non-isotropic nature of room-light. It is interesting to note that these quantum dots take any chance they can get to emit.

### 4.3.3 Green Diode Laser

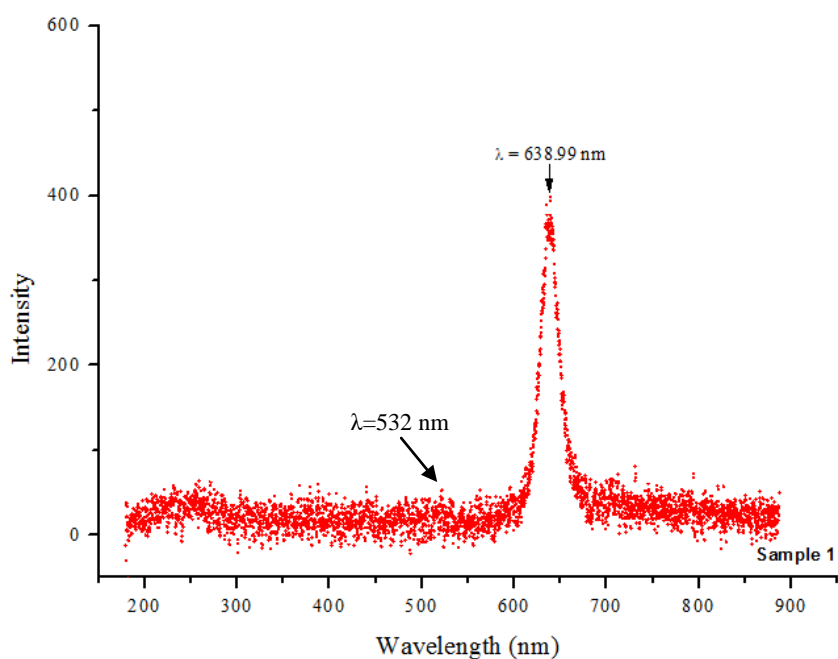


**Figure 9:** First sample of quantum dots under illumination from a green diode laser. The peak emission was at 639 nm and we see evidence of the characteristic green peak at approximately 532 nm.

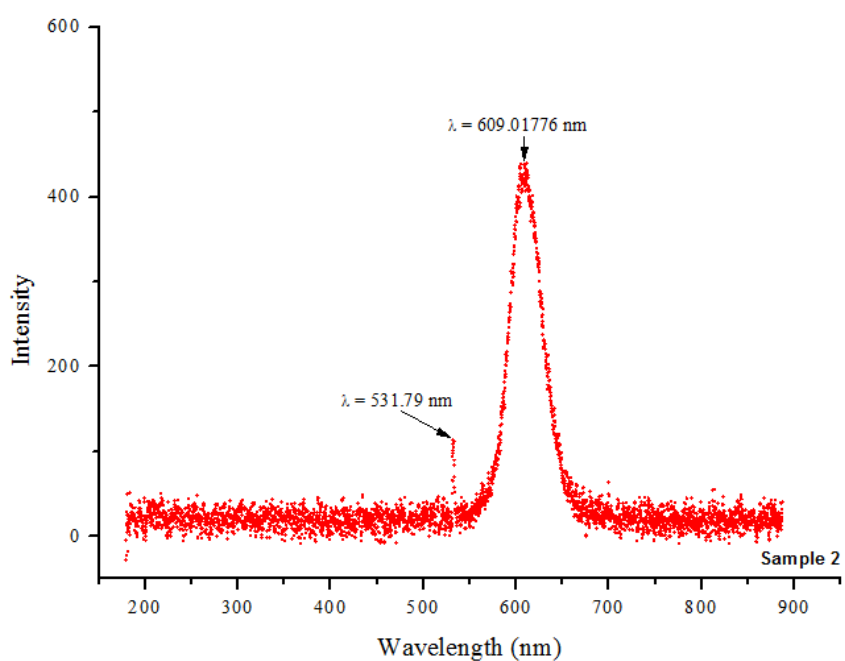


Figure 10: Second sample of quantum dots under illumination from a green diode laser.

#### 4.3.4 HeNe Laser

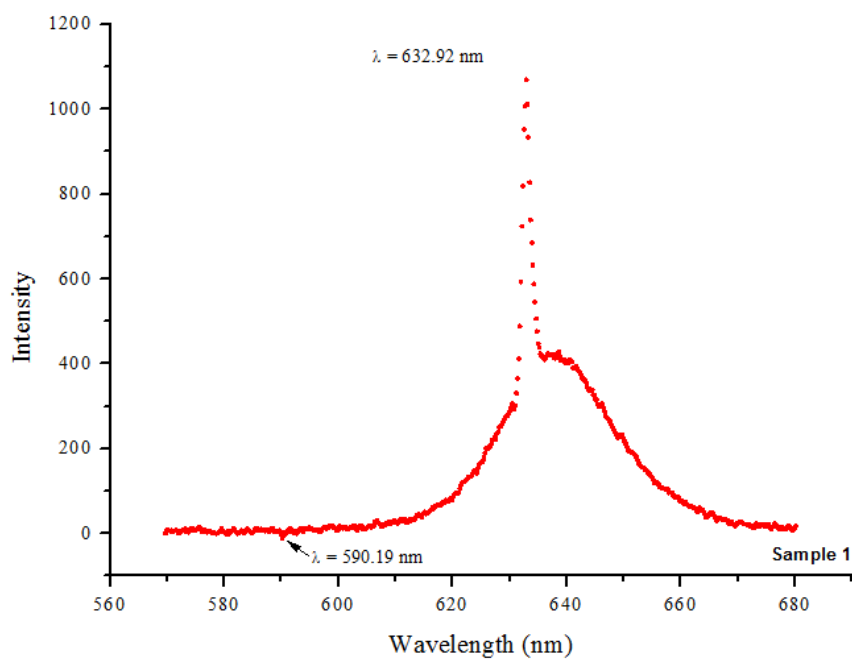


Figure 11: First sample of quantum dots under illumination from a HeNe gas laser. We observe a small absorption trough at approximately 590 nm (the expected trough is at 591 nm).

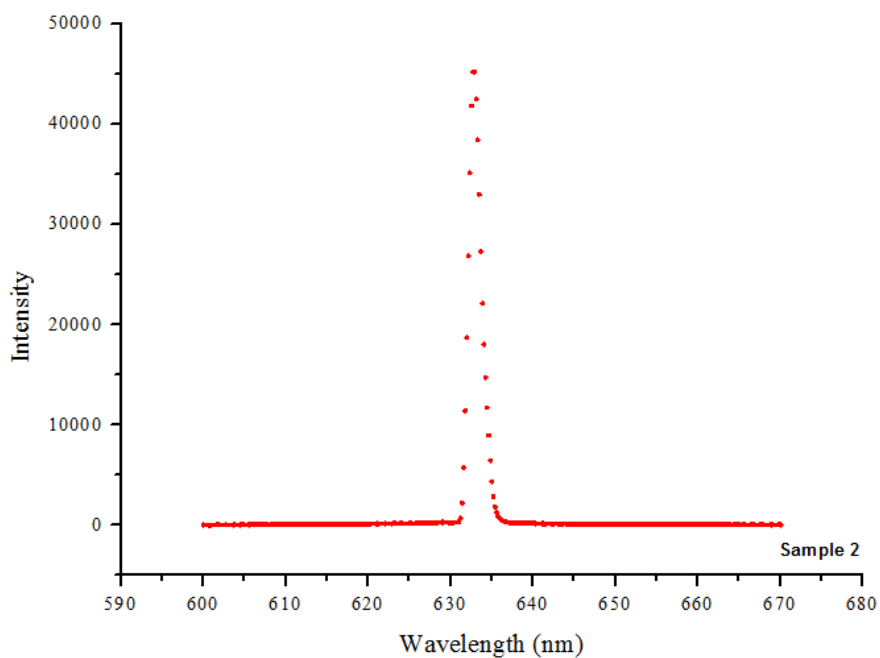


Figure 12: Second sample of quantum dots under illumination from a HeNe gas laser. The large 633 nm peak appears to saturate the spectrum but Fig. 13 below reveals the broad quantum dot emission range near the base of this peak.

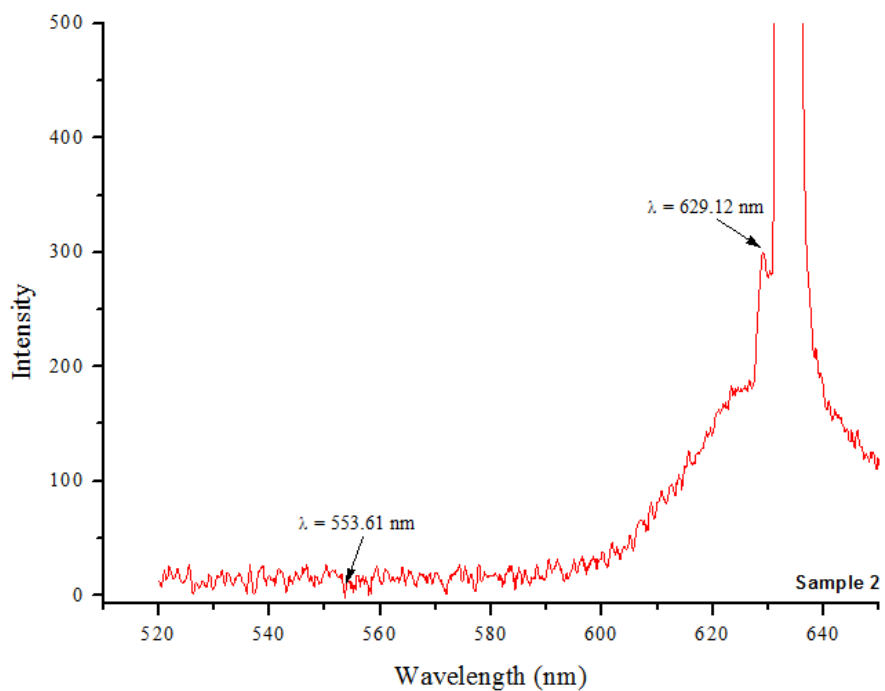


Figure 13: Second sample of quantum dots under illumination from a HeNe gas laser – a close-up of the broad quantum dot emission range near the base of this peak. The unusual 630 nm peak is evident under illumination from a table lamp – see Fig 15 below.

## 4.3.5 Table Lamp

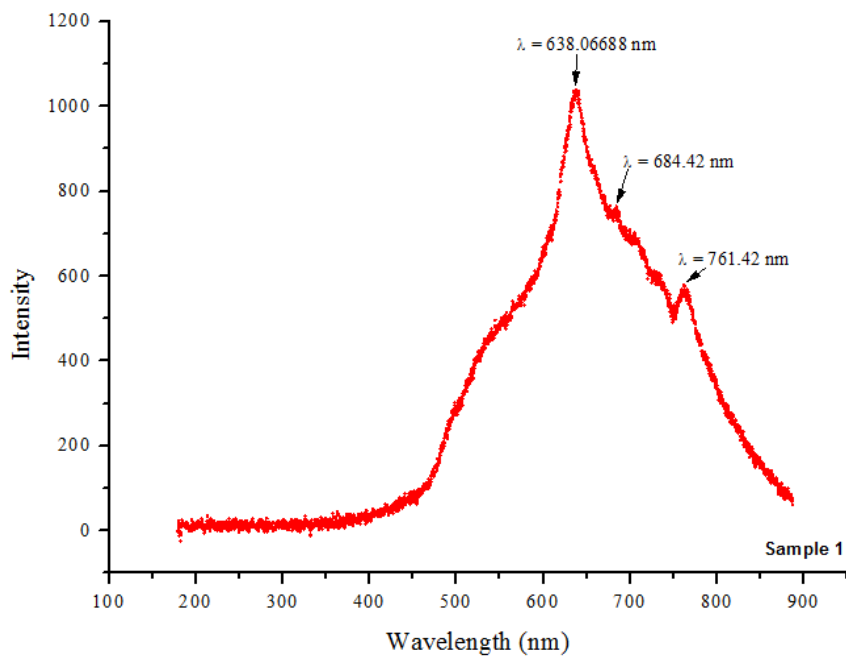


Figure 14: First sample of quantum dots under illumination from a standard table lamp. A broad range of emission and absorption is seen here.

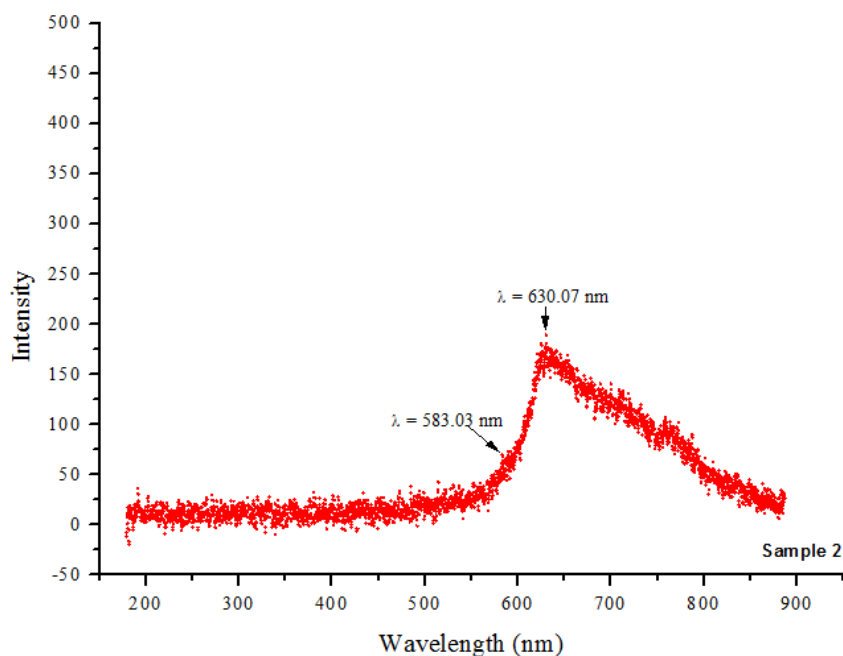


Figure 15: Second sample of quantum dots under illumination from a standard table lamp. The central peak is the 630 nm one which was initially observed under illumination by the HeNe gas laser. We also observe a small 'bump' where we expect a 585 nm emission.

### 4.3.6 Ambient Light

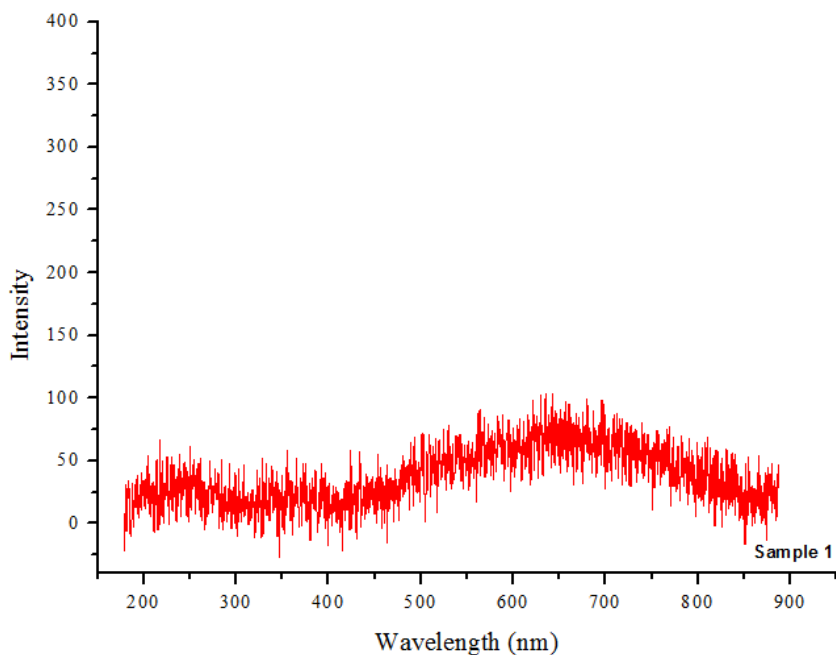


Figure 16: The noisy spectrum of the first quantum dot sample under room-light - even with dim ambient light, these like to emit.

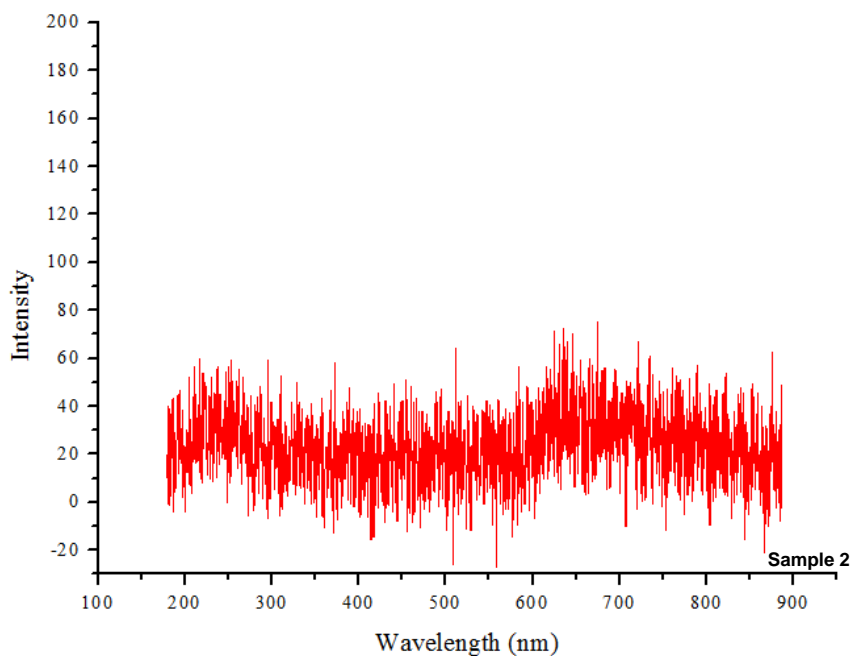


Figure 17: The noisy spectrum of the second quantum dot sample under room-light. We observe a large absorption spike near the expected value of 554 nm and strong absorption at approximately 585 nm (as expected).

## 5. SECTION 2 – OPTICAL TWEEZERS

Optical tweezers experiments have proved their own worth in recent years through the fields of biophysics, photonics and cold atom technologies. Manipulation of micron particles systematically – without environmental interaction – is a powerful experimental skill. Optical trapping forces are typically of the order of tens of piconewtons which is about the same as the forces exerted by molecular motors which power muscles and transport material within cells.<sup>[9]</sup> The first demonstration of an optical tweezers was in 1986 by Ashkin, Chu, Dziedzic, and Bjorkholm.<sup>[11]</sup>

The following collection of background information provides the theoretical basis on which a novel microtapered optical trap can be built.

### 5.1 BACKGROUND THEORY

#### 5.1.1 Fibre Optics

Optical glass fibres have been around for more than 40 years and have since undergone significant fabrication improvements to the point of revolutionising telecommunications. In the late 1960's, the core-cladding glass fibre put an end to the large dispersion and attenuation losses (~500dB/km) which the primitive models suffered. The fibre's core is made from germanium-doped fused silica to give it a slightly higher index of refraction than the surrounding cladding which prominently consists of fused silica.<sup>[10]</sup>

For light rays to be guided through a length of optical fibre, the rays must be totally internal reflected at each core-cladding interface reflection. To initiate the total internal reflection process, the light must first be coupled into the fibre at the appropriate *acceptance angle*. The acceptance angle, when rotated about the longitudinal axis, prescribes a cone of acceptable angles for which the ray will be successfully and efficiently coupled into the fibre. If light rays arrive at the core with an angle greater than the acceptance angle, they will suffer large attenuation losses within the core – these rays decay rapidly and discontinue propagation in the fibre. Examining the cross-section of the acceptance angle, we see that it is trigonometrically given by  $\sin\theta_a$ .

$$n_0 \sin\theta_i = n_2 \sin\theta_t \quad (\text{Snell's Law})$$

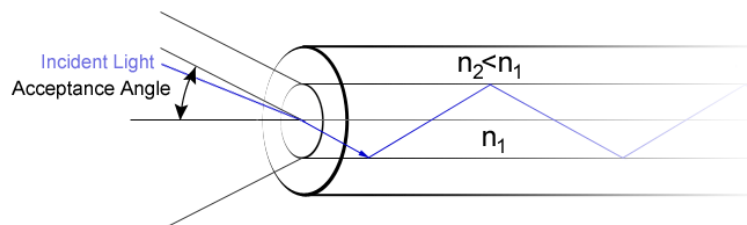


Figure 18: The acceptance angle only allows certain angles of incident light to be coupled into the fibre core.

For angles larger than the critical angle,  $\theta_c$ , the sine is not defined if  $n_2 < n_1$  –

$$\theta_c = \sin^{-1}\left(\frac{n_2}{n_1}\right)$$

For a multi-mode fibre, it is uncomplicated to derive an equation for the acceptance angle. When a ray of light is incident on a fibre end, Snell's law at the environment-core interface is  $n_0 \sin\theta_i = n_1 \sin\theta_t$ . For total internal reflection to occur immediately, the angle at which the ray is transmitted must be  $90^\circ - \theta_c$ . Thus –

$$\begin{aligned} n_0 \sin\theta_i &= n_1 \sin(90^\circ - \theta_c) = n_1 \cos\theta_c \\ \Rightarrow \frac{n_0}{n_1} \sin\theta_i &= \cos\theta_c \\ \Rightarrow \left(\frac{n_0}{n_1}\right)^2 \sin^2\theta_i &= \cos^2\theta_c = 1 - \sin^2\theta_c = 1 - \frac{n_2^2}{n_1^2} \\ \Rightarrow n_0^2 \sin^2\theta_i &= n_1^2 - n_2^2 \\ \Rightarrow \text{Numerical Aperture} &= n_0 \sin\theta_i = \sqrt{n_1^2 - n_2^2} \end{aligned}$$

This is the numerical aperture (NA) – the square of which is a measurement of the light-gathering power of the fibre. For single-mode fibres, the NA cannot be determined purely through the refractive indices – it depends on wavelength. For example, with a Gaussian beam coupled into a single-mode fibre, the width of the beam profile must be calculated and used directly in calculating  $\sin\theta_i = \text{width} \div \text{distance between detector and start of laser beam}$ . The NA of a single-mode fibre is dependent on wavelength. If light of a wavelength  $\lambda_1$  is coupled into a fibre of a certain wavelength  $\lambda_0$ , ( $\lambda_0 \neq \lambda_1$ ), the core can no longer restrict the transmission to a single mode. The core width of a multimode fibre is typically 50-60  $\mu\text{m}$  while the core of a single mode fibre is 8-10  $\mu\text{m}$ .

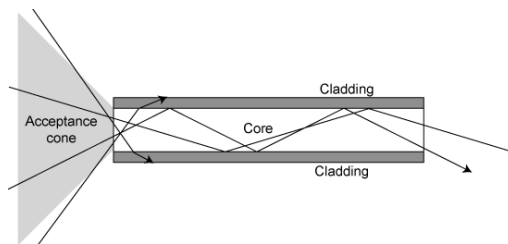


**Figure 19: A multi-mode fibre can carry many different wavelengths due to its larger core diameter.**

### 5.1.2 The Evanescent Field

We now introduce a phenomenon associated with total internal reflection of planar electromagnetic waves which we aim to take advantage of to create an optical trapping field.

When a light beam travels from a dense medium into a rare medium, a reduction in angle of propagation of the beam with respect to the normal to the surface arises. This is refraction of light.

Consider a hemispherical glass block in air with a light ray incident on the block's back wall as shown in Figure 21. Above a certain angle of incident, the ray will be totally internally reflected – the ray will not continue propagation in air. The phenomenon of TIR was recognised first by Newton, but it was Quincke in 1966 and Bose in 1897 that performed more precise experiments investigating the transfer of light into the second medium as a function of incident angle and wavelength (Quincke 1966a, Quincke 1966b, Bose 1897, Hall 1902).<sup>[11]</sup> A more complete treatment of the physics behind evanescent fields requires the electromagnetism formalism rather than the simplistic ray optics approach. This is demonstrated below.

Consider a two-medium system with a definite interface dividing the areas of non-equal refractive indices,  $n_1$  and  $n_2$ . We chose the  $z$  plane to lie along the interface and the  $x$  plane to be directed from the medium of refractive index  $n_1$  to the medium with  $n_2$ . The  $y$  plane is directed “out of the page” and therefore the  $y = 0$  plane is the plane of incidence. We further assume the two media to be non-absorbing, isotropic and homogeneous. The incident, reflected and transmitted electric fields are described in a most general sense by –

$$\mathbf{E}_i = \mathbf{E}_{i0} e^{i(\omega t - \mathbf{k}_i \cdot \mathbf{r})}, \mathbf{E}_r = \mathbf{E}_{r0} e^{i(\omega t - \mathbf{k}_r \cdot \mathbf{r})}, \mathbf{E}_t = \mathbf{E}_{t0} e^{i(\omega t - \mathbf{k}_t \cdot \mathbf{r})}$$

Here, the complex amplitudes  $\mathbf{E}_{i0}$ ,  $\mathbf{E}_{r0}$ ,  $\mathbf{E}_{t0}$  are space and time-independent. The wave-vector associated with the incident wave,  $\mathbf{k}_i$ , is parallel to the  $x$ - $z$  plane and so we have  $k_{i,y} = 0$ . Expanding the dot product of the wave-vector and position vector,  $\mathbf{r}$ , we have –

$$\mathbf{k} \cdot \mathbf{r} = k_x x + k_y y + k_z z = k_y y + k_z z \text{ because the interface is @ } x = 0$$

For  $\mathbf{E}_i$  in the plane of incidence, since the  $z$  component is tangential to the surface, the  $E_z$  components must be continuous across the interface. Therefore we obtain consequences [1], [2] and [3] –

$$\Rightarrow E_{i,z} + E_{r,z} = E_{t,z} \Rightarrow \begin{cases} \therefore \omega_i = \omega_r = \omega_t \text{ [1]} \\ \therefore k_{i,y} = k_{t,y} = k_{r,y} = 0 \text{ because } k_{i,y} = 0 \text{ [2]} \\ \therefore k_{i,z} = k_{t,z} = k_{r,z} \text{ [3]} \end{cases}$$

From [2], we see that  $k_i \sin \theta_i = k_t \sin \theta_t = k_r \sin \theta_r$ , and so:  $\theta_i = \theta_r$  (The Law of Reflection). Thus –

$$\Rightarrow \frac{\sin \theta_i}{\sin \theta_t} = \frac{k_t}{k_i} = \frac{\sqrt{\epsilon_2 \mu_2}}{\sqrt{\epsilon_1 \mu_1}} = \frac{n_2}{n_1}$$

This is Snell's Law of Refraction. If  $n_2 < n_1$  then  $\sin \theta_t$  will be greater than 1 if  $\theta_i > \theta_c$  where  $\theta_c = \sin^{-1}(n_2/n_1)$  as before. Note that we can write  $\cos^2 \theta_t$  as follows:

$$\cos^2 \theta_t = 1 - \sin^2 \theta_t = - \left( \frac{n_1^2}{n_2^2} \sin^2 \theta_i - 1 \right) > 0 \text{ when } \theta_i > \theta_c$$

$$\therefore \cos \theta_t = -i \sqrt{\frac{n_1^2}{n_2^2} \sin^2 \theta_i - 1}$$

Note that if we had taken the positive square root above, i.e.  $+i\sqrt{\dots}$  then we would have an exponentially increasing field in the second medium – which is clearly not physically realistic! We consider specifically the case of  $s$  polarization where the transmission coefficient can be shown to be.<sup>[12]</sup>

$$t_s = \frac{E_{t0}}{E_{i0}} = 1 + r_s = \frac{2n_1 \cos\theta_i}{n_1 \cos\theta_i + n_2 \cos\theta_t}$$

The transmission coefficient is now a complex quantity, and noting the fact that it can therefore be written as  $t_s = |t_s|e^{i\alpha}$  (where  $\alpha$  is some phase constant) we can write the transmitted electric field as:

$$\mathbf{E}_t = |t_s|E_{i0}e^{i[\omega t - k_t(x\cos\theta_t + z\sin\theta_t) + \alpha]}\hat{\mathbf{y}}$$

Substituting in for  $\cos\theta_t$ ,  $\sin\theta_t$  and  $k_t = \frac{\omega}{c}n_2$  we get –

$$\mathbf{E}_t = |t_s|E_i e^{-d_p x} e^{i[\omega t - \omega \frac{n_1}{c} z \sin\theta_i + \alpha]}$$

This represents a wave which propagates in the  $z$  direction. The amplitude of the electric field decreases exponentially, in the  $x$  direction, as the distance from the interface increases. The parameter  $d_p$  is the *penetration depth* of the evanescent field which reflects the amplitude-decay of the evanescent field as we move away from the interface. The penetration depth ranges from infinity to  $\lambda/2\pi\sqrt{n_1^2 - n_2^2}$  –

$$d_p = \frac{\lambda}{2\pi\sqrt{n_1^2 \sin^2\theta_i - n_2^2}}$$

Only a limited part of the second medium “sees” the evanescent field. When the incident field is  $s$  polarized the evanescent field is purely transverse to the direction of propagation. In  $p$  polarization, the electric field has two non-zero components with a phase difference equal to  $\pi/2$ . The extremity of this vector describes an ellipse as time evolves.

$$\mathbf{H}_t = \left[ -\frac{n_1 \sin\theta_i}{n_2} \hat{\mathbf{x}} - i \sqrt{\frac{n_1^2}{n_2^2} \sin^2\theta_i - 1} \hat{\mathbf{z}} \right] \times \frac{|t_s|}{Z_t} E_i e^{-d_p x} e^{i[\omega t - \omega \frac{n_1}{c} z \sin\theta_i + \alpha]}$$

The  $\mathcal{R}e$  parts of  $\mathbf{E}_t$  and  $\mathbf{H}_t$  shown above describe the actual electromagnetic fields – thus, the exponential factors are separated into their respective cosine and sine components. If we examine the average energy flow along the  $x$  direction,  $\langle S_x \rangle = \langle E_y H_z \rangle$ , we see that it equals zero. However, if we look at  $\langle S_z \rangle$  we obtain –

$$\langle S_z \rangle = \langle -E_y H_x \rangle = \frac{n_1 \sin\theta_i}{2n_2} |t_s|^2 \frac{E_i^2}{Z_2} e^{-2d_p x}$$

Therefore, there *is* power flowing along the  $z$  axis in the second medium. Over a half-period, the flux is also zero. In contrast, over a quarter period, the average flux,  $\langle S_z \rangle$ , has *non-zero* values. At the next quarter-period, the signs in the equation are reversed. Hence, even if a wave is present in the second medium, the net energy flux through the interface is zero on average.<sup>[13]</sup>

Evanescent fields are further characterised by a longitudinal shift of the light beam reflected after TIR as predicted by Newton and verified F. Goos and H. Hänchen in 1947.<sup>[14]</sup> This reaffirms the idea that the evanescent wave is a “surface wave” – illustrated in Figure 20 below.

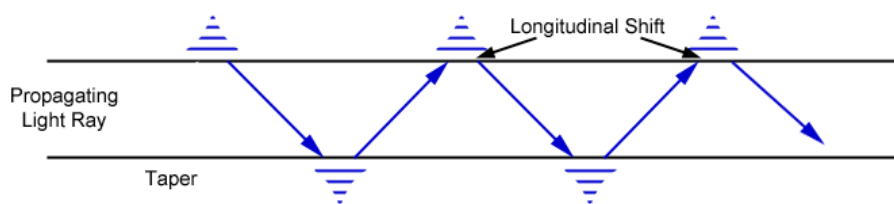


Figure 20: The Goos-Hänchen longitudinal beam-shift under TIR.

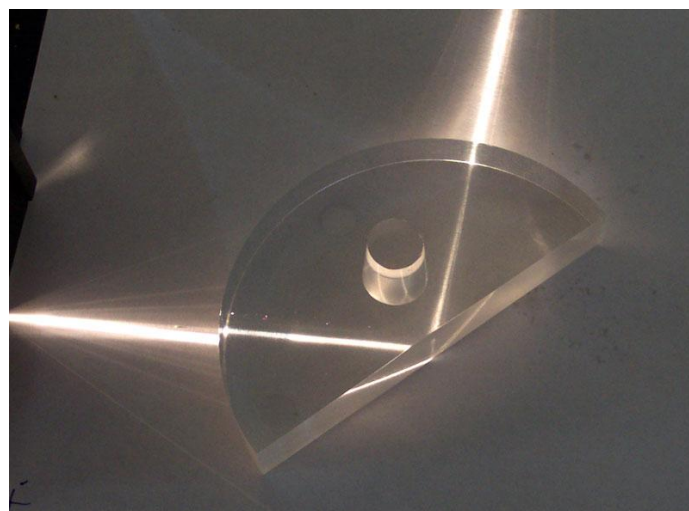


Figure 21: Total internal reflection in a hemispherical glass block. The evanescent wave is generated along the back wall and, under these conditions, extends for  $\sim 60 \mu\text{m}$ . Copyright © Fir0002.

### 5.1.3 The Generation of Evanescent Fields from Optical Fibre Tapers

We can approximate the waves travelling in a fibre optic cable as planar and thus the evanescent field exists on a very short distance scale within the cladding. To enhance this evanescent field, the fibre cladding can be stripped off so that the surrounding air ( $n \approx 1$ ) effectively becomes the cladding and we obtain a much stronger evanescent field – the penetration depth of which would be  $\sim 100 \text{ nm}$  at a wavelength of  $1300 \text{ nm}$ .

To further improve this penetration depth, the exposed core can be heated and “stretched” so that it has a relatively small diameter compared to that of the lengths of cladded fibre (“pigtailed”) at either end.

Popular methods of taper creation include  $\text{CO}_2$  laser heating, flame heating, and the use of a *microfurnace*.<sup>[15][16][17]</sup> The microfurnace method has achieved taper diameters of below  $100 \text{ nm}$ . The method used during this project was the flame heating where a length of fibre is mounted over a hot, narrow flame and stretched at a rate controlled using computerised motors.

It is important to note that, for each method, the adiabaticity criterion<sup>[18]</sup> must be satisfied to prevent re-coupling from the fundamental mode ( $\text{HE}_{11}$ ) to higher order modes within the fibre, or

radiative losses of the fundamental mode. If we examine the profile of a taper with length directed along the  $\hat{z}$  direction (see Figure 22 below), we have that –

$$\tan\Omega = \left| \frac{dr}{dz} \right| \leq \frac{\rho(z)}{2\pi} [\beta_1(z) - \beta_2(z)]$$

Where  $\beta_1(z)$  and  $\beta_2(z)$  are the local propagation constants of the fundamental mode and the next closest mode, respectively. The tangent of the local taper angle,  $\Omega$ , is given trigonometrically by  $dr/dz$  and  $\rho(z)$  is the distance-varying taper radius. This equation can be solved numerically.

The core guidance parameter,  $V = ka \sqrt{n_{core}^2 - n_{clad}^2}$ , evaluated for a taper waist radius of 1  $\mu\text{m}$  at a wavelength of 1460 nm gives a value of  $\approx 4.2$  which is greater than 2.405 indicating that the taper is multi-moded. A single-mode taper is feasible only with a taper of diameter less than 1  $\mu\text{m}$ .

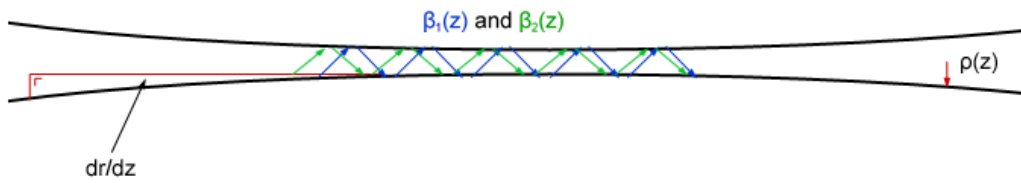


Figure 22: Taper geometry to describe the adiabaticity criterion.

As far back as 1604, Johannes Kepler suggested that a comet's tail might be generated by the refraction of sunlight travelling through the comet's head. (Schechner Genuth, 1997) The pressure of the sunlight forced the tail away from the sun. It was Maxwell who eventually reinforced this idea that light exerts a *radiation pressure* – he wrote, “In a medium in which waves are propagated there is a pressure in the direction normal to the waves, and numerically equal to the energy in a unit volume.” In other words, radiation pressure is a force per unit area on an object due to the change in momentum of light.

All light consists of photons with momentum  $\mathbf{p}$ . For light of specific wavelength  $\lambda$ , the magnitude of the momentum of a single photon is given by –

$$p = \frac{h}{\lambda}$$

The intensity of the light is determined by the number of photons passing through a given area per unit time. The momentum flux of photons from light of intensity given by the Poynting vector  $\mathbf{S}$  is –

$$\frac{d}{dt} (d\mathbf{P}) = \frac{n}{c} \mathbf{S} dA$$

Here,  $n$  is the index of refraction,  $c$  is the speed of light,  $\mathbf{P}$  is the total momentum of the photons and  $dA$  is an element of area normal to  $\mathbf{S}$ . The total force on an object due to refraction of light is therefore:

$$\mathbf{F} = \frac{n}{c} \iint (\mathbf{S}_{in} - \mathbf{S}_{out}) dA$$

Thus, if the light coming into a dielectric from a medium of index  $n$  is deflected, changing the direction of  $\mathbf{S}$  when it exits the dielectric, there is a finite force exerted on the object.

For example, we can calculate the force due to the change in momentum of light reflecting off of a mirror. In this case,  $\mathbf{S}_{in} = -\mathbf{S}_{out}$ , so  $\mathbf{F} = \frac{2n}{c} \iint \mathbf{S}_{in} dA$ . The integral is the total power of the light, which is usually expressed in Watts. We assume perfect reflectivity so the force is given by  $F=2nW/c$ , where  $W$  is the intensity of the light in Watts.<sup>[19]</sup> More generally, the corresponding radiation pressure force on a perfect absorber will be  $F$  and on a perfect reflector it will be  $2F$ .

If all the intensity of a 60 W light bulb were focused onto a mirror, the force due to radiation pressure would be  $4 \times 10^{-7}$  N. If a 1 kg mirror exerts a force on a scale of 9.8 N, the additional weight due to radiation pressure is clearly negligible. Objects for which this radiation pressure would be significant would have to weigh less than 1  $\mu\text{g}$ .

In optical tweezers experiments, the radiation pressure is provided by laser light and the objects to be manipulated are very small. Micron-sized polystyrene spheres of uniform diameter are easily obtained and can be trapped using the forces described in the equation above.

#### 5.1.4 Trapping Micron Particles

It should be noted that to develop a complete theoretical understanding of optical trapping there are in fact two limiting cases for which the forces on the trapping particle can be calculated. The

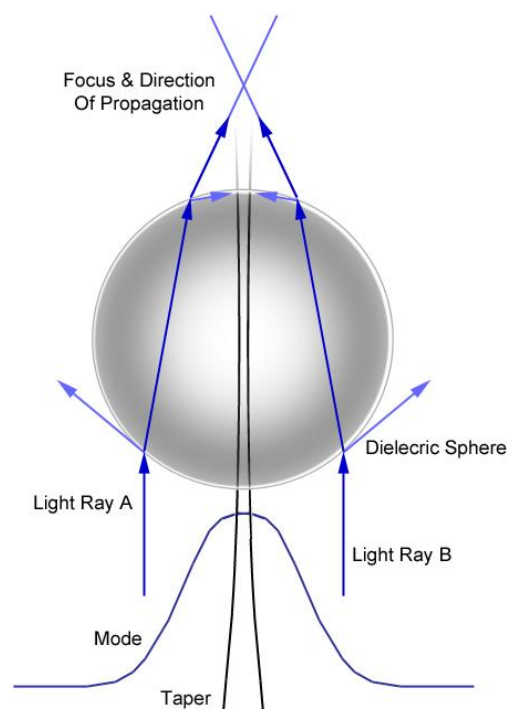


**Figure 23: In the Mie regime ( $d \gg \lambda$ ) the scattering and gradient forces act together to propel the sphere in the direction of the electric field and towards the point of maximum intensity.**

intermediate case where the wavelength of the trapping light is comparable with the dimensions of the sphere requires treatment with Maxwell's equations, appropriate boundary conditions and considerations from the *Generalized Lorenz-Mie Theory* (GLMT). It is unfortunate that in most trapping experiments, trapping particles of dimensions  $\sim 1 \mu\text{m}$  are chosen for ease of microscopy and laser light of  $\sim 1 \mu\text{m}$  is chosen due to commercial availability. Further, interesting biological specimens such as yeast, organelles and bacteria are roughly all of the same order as the wavelength of trapping light.

The trapping of spherical particles with dimensions of order  $10\lambda$  and greater can be understood simplistically using a ray optics approach (Figure 23). In this regime, the diameter of the particle,  $d$ , is much greater than the wavelength of the light incident on the particle-environment interface – this satisfies the Mie scattering conditions. We track two light rays through the sphere when it positioned symmetrically with respect to an ideal Gaussian mode travelling through a single-mode taper. For ease of illustration, the sphere has been enlarged in comparison to the taper – realistically, the taper width

and sphere diameter are quite comparable. On entry and exit, the photons comprising light ray *A* undergo refraction and reflection. This constitutes a change in the Poynting vector and thus a finite force is exerted on the sphere. Due to the symmetric position of the sphere with respect to the position of maximum laser light intensity in this case, an equal and opposite force is provided by light ray *B* due to reflection and refraction of light. Thus, the force remains directed centrally along the taper – the sphere is propelled along with the electric field. It is easy to imagine a sphere on the left or right of the taper – it experiences a restoring force towards the taper centre and position of maximum laser light intensity. For a sphere positioned on the left, light ray *B* would provide a greater force than light ray *A*, and vice versa for a sphere to the right of the taper.

Fundamentally, there are two forces at play in this ray optics approach – a scattering force and gradient force. These are not independently identifiable because the ray optics approach is valid for sphere diameters  $\sim 10\lambda$  and greater so that optical forces become independent of the size of the sphere. For spheres of diameter  $\ll$  the wavelength of the incident light, the Rayleigh scattering conditions are satisfied. In this regime, we consider the sphere as a ‘point’ dipole so that the scattering and gradient forces are readily separable – the electromagnetic field within the particle is uniform. The scattering force is due to absorption and re-radiation of light by the point dipole. For a sphere with radius *r*, the scattering force is –

$$\mathbf{F}_{scatt} = \frac{I_0 \sigma n_m}{c}$$

$$\sigma = \frac{128\pi^5 r^6}{3\lambda^4} \left( \frac{m^2 - 1}{m^2 + 2} \right)^2$$

Here,  $I_0$  is the intensity of the incident light,  $\sigma$  is the scattering cross section of the sphere,  $n_m$  is the index of refraction of the medium,  $c$  is the speed of light in vacuum and  $m$  is the ratio of the index of refraction of the particle to the index of the medium ( $n_p/n_m$ ). The scattering force, just as described above for the Mie regime ( $d \gg \lambda$ ), is in the direction of the propagating electric field within the taper and is greatest at the point of maximum intensity.

A gradient force arises due to the interaction of the induced dipole with the inhomogeneous evanescent field. This takes into account the polarizability,  $\alpha$ , of the particle as a dipole. The gradient force is proportional to the intensity gradient –

$$\mathbf{F}_{grad} = \frac{2\pi\alpha}{cn_m^2} \nabla I_0$$

$$\alpha = n_m^2 r^3 \left( \frac{m^2 - 1}{m^2 + 2} \right)$$

When the particle is optically denser than the surrounding medium ( $m$  is then greater than unity), this force points “up” the gradient (Neuman & Block, 2004).<sup>[20]</sup>

An amalgamation of the Rayleigh and Mie theories do not explain the intermediate case where  $d \sim \lambda$ . Many attempts have been made to generalize the Lorenz-Mie theory to the scattering of a planar wave off of spherical surface (Weber & Hirleman, 1988)<sup>[21]</sup> but these do not completely account for the physics behind intermediate optical trapping. One group extended the Rayleigh regime to larger particles using second-order scattering terms. The trapped spheres, in this case, would have to introduce a phase shift less than  $\pi/3$ . For polystyrene beads in water, the upper diameter limit is about

$0.7\lambda$  for this extended-Rayleigh approach. The experimental results of these trapping experiments have compared well with theory. A full, general theory has yet to be explored.

### 5.1.5 On-Resonance Spheres in the Evanescent Field

The existence of *whispering gallery modes* (WGMs) has been observed in optically trapped polystyrene spheres (Brambilla, Murugan, Wilkinson, & Richardson, 2007)<sup>[5]</sup> as well as hollow glass microspheres (see Figure 24 below)<sup>[3]</sup>. WGMs arise due to TIR of certain wavelengths at the internal boundary of the sphere. The resulting modes are described by a mode number,  $n$ , and mode order,  $l$ , to describe the number of wavelengths around the circumference of the sphere and the number of maxima in the radial dependence of the field in the sphere, respectively. Under optical trapping, we would expect to see on-resonance beads travelling faster than those beads which are off-resonance.

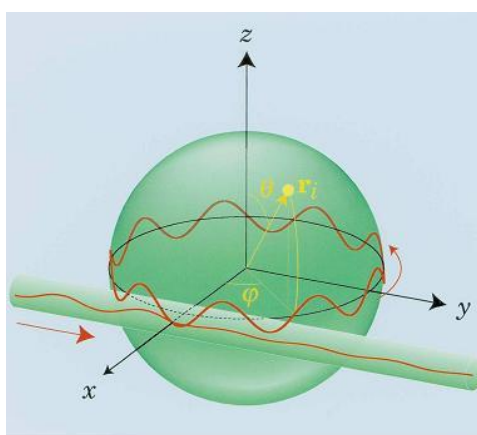


Figure 24: From Arnold et al. *Optics Letters* 28,272 (2003), Fig.1. A protein molecule sits at position  $r_i$  on the surface of a sphere near an “eroded” optical fibre core. Laser light is coupled into the sphere from the fibre.

### 5.1.6 Semiconductor Diode Laser in Trapping Experiments

The use of semiconductor diode lasers is widespread in fibre optic applications because of their relatively high power, spectral purity and coupling efficiency (which is  $\approx 100\%$ ). They can also be modulated at very rapid rates making them ideal for acousto-optic applications. They were invented in 1962 following the development of the LED.<sup>[22]</sup> Initially, because these were based on homojunctions, they had to be operated at about 100K in CW mode only. It was realised that a heterojunction would allowed lower threshold current and room temperature operation.

A semiconductor laser’s ability to convert electrical current into laser depends on two factors – junction temperature and pump current. The amount of current required before the laser reaches steady stimulated emission is known as the threshold current,  $I_{th}$ . The power output of a diode laser depends on junction temperature and pump current in the following ways –

$$I_{th}(T) = I_{th}(T_1)e^{\frac{T-T_1}{T_0}}$$

$$P = (I - I_{th}) \frac{dP}{dI}$$

Thus we see a strong exponential dependence between the junction temperature and the resulting light intensity (see Figure ). In most practical applications, we aim to keep the temperature constant using a temperature controller or *TEC*.

We can characterise a diode laser with an LI curve – a plot of power against current (or, equivalently voltage against current). We obtain a plot similar to that shown in Figure 26. The threshold current is found by extrapolating the linear portion to  $V = 0$ . The slope of the linear segment above threshold is related to *external differential quantum efficiency*,  $\eta_{diff}$ , through the equation –

$$\eta_{diff} = \frac{\lambda_0 q}{hc} \frac{dP}{dI}$$

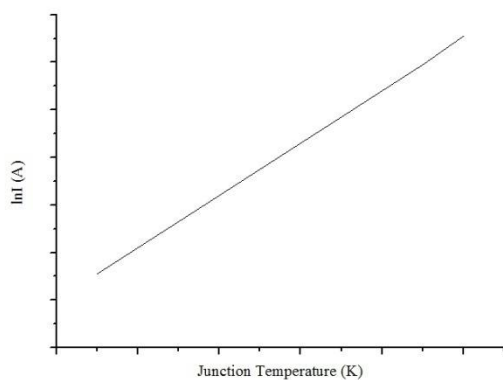


Figure 25: Log plot of pump current as a function of junction temperature.

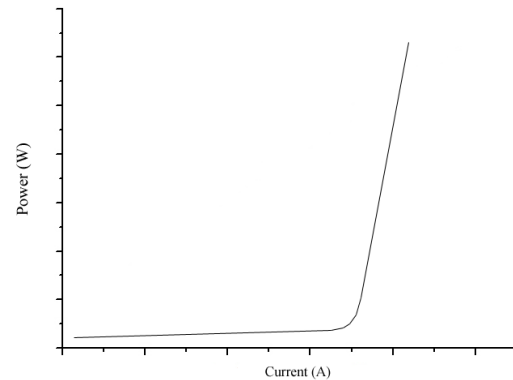


Figure 26: Power against current for a diode laser.

## 5.2 EXPERIMENTAL PROCEDURE

### 5.2.1 Characterisation of Diode Laser with LI Curve

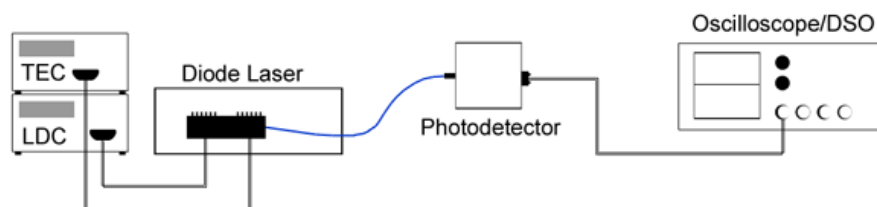


Figure 27: Apparatus used to characterise diode laser.

To investigate the LI curve for the 1460 nm, 140 mW diode laser (see Appendix A for specification sheets), the apparatus shown in Figure 27 was used to measure the output voltage signal from the laser. The TEC and LDC were set to  $\approx 20$  °C and 0.17 mA respectively. This non-zero zero-point current provided the initial data point on the oscilloscope screen. The current was increased in 2 mA intervals and the resulting DC signal was noted from the oscilloscope screen. This procedure was repeated until the DC signal became saturated. A voltage versus pump current plot was then generated.

For comparison, the diode laser was then connected to an optical spectrum analyser (OSA). The pump current, initially set to 0.17 mA, was again increased in 2 mA intervals. The spectrum and peak power was read from the OSA screen at each point to generate a power versus pump current plot.

By extrapolating the resulting linear segments on the power versus current and voltage versus current curves, a value for the threshold current was determined with appropriate error bounds. These plots are displayed and analysed in the Discussion.

### 5.2.2 Optical Tweezers – Set-Up 1

(See Figure 28 for a schematic diagram and Figure 29 and 30 for photographs of the apparatus.) A  $\sim 1$   $\mu\text{m}$  taper was created using 1060 nm single-mode fibre with the heat-and-pull rig. To aid cleaving and splicing, long pigtailed fibres were used. The fibre measured approximately 1 m in length. One end of the fibre was stripped of its cladding, cleaned liberally with ethanol and cleaved. The same procedure was followed for the commercial grade fibre connected to the diode laser. Both ends were then spliced using the fusion splicer. The resulting transmission loss was  $\approx 0.02$  dB. The LDC and TEC were switched on and set to  $\sim 100$  mA and 20 °C respectively. Using an IR viewing card, the free pigtail was aimed at the sensing medium to verify that light was propagating through the entire length of fibre. The total transmission loss due to taper and splice was approximately 50%. The stage was transported to an optical lab bench where a CCD camera and 100 $\times$  oil immersion objective were set up. A glass slide (76 mm  $\times$  25.4 mm  $\times$  1 mm) was cleaned liberally with methanol and clamp to a translation stage close to the taper. The slide was carefully moved up towards the taper and positioned lengthways so that approximately 5 mm of the fibre's unstrapped cladding overlapped either end of

the slide. When the taper and slide were aligned correctly and almost in contact, clear varnish was applied to either end of the taper to fix it to the glass. While the varnish dried, a sample of water and beads was prepared. This was done by putting ~20 ml of deionised water into a plastic container and using a micropipette to transfer 5  $\mu\text{m}$  beads into the water. The suspension was stirred to prevent the beads clumping. A clean pipette was used to drop the water-bead suspension onto the taper and glass slide. The sample depth was approximately 2 mm.

The taper was detached from the stage posts when the nail varnish had dried. The stage was removed so that full deflections of the translation stage could be made.

Due to the small working distance of the objective (0.17 mm) a cover slip for the sample was not used. Instead, the taper and sample were raised towards the objective until the lens entered the sample.

A CCD camera was placed directly on top of the objective. To use the camera under these high-magnification conditions, a number of modifications had to be made to the unit. The camera had an audio connector which was immediately neglected. The connectors on the power source leads and video leads were cut off and approximately 1" of insulation was stripped from the leads. The ground wires from the audio and power lead were identified and soldered to the ground of a BNC connector. The signal wire from the audio lead was soldered to the signal connection on the BNC connector. The BNC connector was connected to a BNC cable from a monitor and the CCD camera was connected to a 12V power supply.

Using very fine movements, an image of the taper and beads was focused on the monitor screen. A video of the Brownian motion of the polystyrene beads was recorded by routing the cameras BNC cable to a computer with *Windows Movie Maker* software.

The laser drivers were then powered on. The current was set to 0.17 mA and the temperature was set to ~20 °C. The movement of the beads were observed on the monitor, and then, by connecting the BNC cable to a computer, *Movie Maker* was used to record the bead movements. Image analysis could then be performed on the beads using *Scion Image*.

### 5.2.3 Optical Tweezers – Set-Up 2

(See Figure 28 for a schematic diagram and Figure 29 and 30 for photographs of the apparatus.) A ~1  $\mu\text{m}$  taper was created using 780 nm single-mode fibre with the heat-and-pull rig. To aid cleaving and splicing, long pigtailed were used once again so that the fibre measured approximately 1 m in length. The entire stage unit was transported to the microscope stage.

One end of the fibre was stripped of its cladding, cleaned liberally with ethanol and cleaved. The same procedure was followed for the commercial grade fibre connected to the diode laser. Both ends were then spliced using the fusion splicer. The resulting transmission loss was  $\approx 0.02$  dB. The LDC and TEC were switched on and set to ~100 mA and 20 °C respectively. Using an IR viewing card, the free pigtail was aimed at the sensing medium to verify that light was propagating through the entire length of fibre. The total transmission loss due to taper and splice was approximately 50%. The laser drivers were switched off in order to correctly place the sample.

The dark hood of the microscope was placed over the taper and stage to minimise ambient light and dirt on the taper. The taper was located and focused with a 20× objective and using a scale etched on the eyepiece, the minimum diameter of the taper was estimated to be 1  $\mu\text{m}$ .

A sample of glycerol and deionised water was prepared in a ratio of 1:2 in volume. The solution was stirred in a plastic container until the glycerol had visibly mixed with the water. A micropipette was used to transfer a small portion of polystyrene beads to the sample. The sample was stirred again to promote a uniform arrangement of beads throughout.

A glass slide was cleaned using lens wipes and methanol and transferred to the translation stage in front of the taper. Using a clean pipette, the bead suspension was dropped onto the glass slide. The slide was then positioned under the taper and moved slowly towards it until the taper lay within the sample. Using the microscope, whose focus had not been adjusted since viewing the taper, focused beads were observed indicating that the beads lay in approximately the same horizontal plane as the taper. It was verified that there was an adequate arrangement of beads surrounding the taper by scrolling along the taper with the microscope.

The LDC and TEC were switched on once again with the TEC indicating  $\sim 20$  °C and the LDC initially at 0.17 mA – well below the threshold current. The CCD camera connected to the microscope was switched on and sent to a monitor. The pump current was increased about the threshold current and varied within the 50 mA – 490 mA range. Movements of the beads were then recorded using a connection to a computer with *Windows Movie Maker* software.

To systematically control the beads, an intensity modulator was connected to the LDC. Various input signals (square, triangular and sinusoidal) were chosen for different frequency ranges and videos of bead movements were recorded with *Movie Maker*.

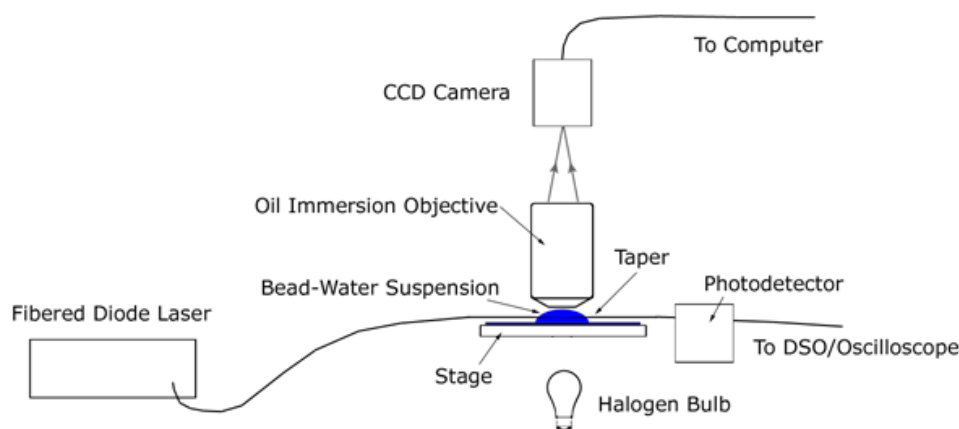


**Figure 28:** Schematic diagram of the microtaper-based optical tweezers. The diode laser is driven by a TEC and LDC (not shown) and the taper intersects a sample of water-glycerol-bead suspension. A computer is used to frame-grab images from the CCD camera and objective.

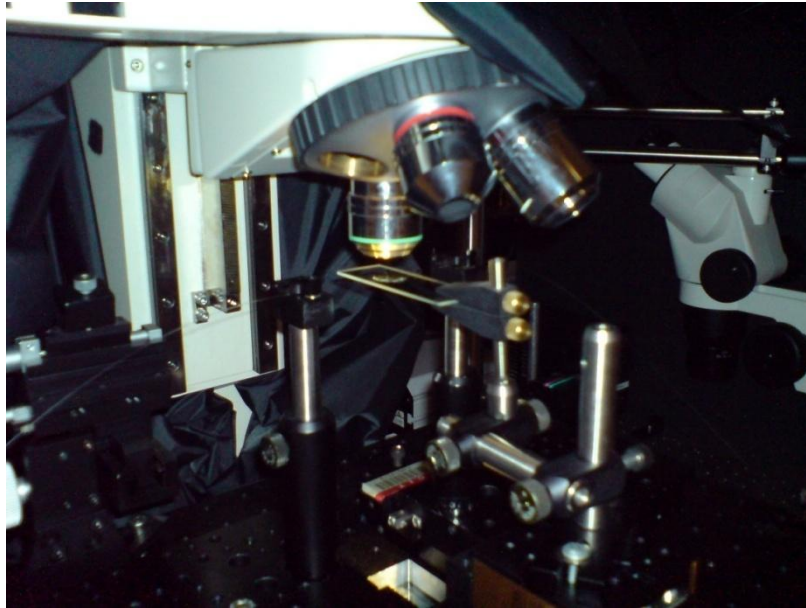


Figure 29: Microscope objective and glass slide with bead-water-glycerol sample.

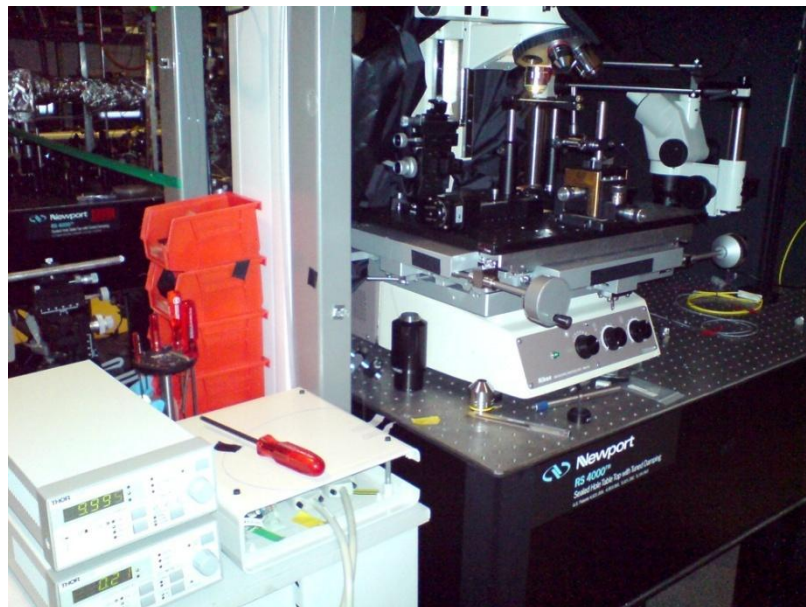


Figure 30: Overview of the optical bench with the laser drivers on the bottom left beside the diode laser.

## 5.3 RESULTS & DISCUSSION

### 5.3.1 Characterisation of Diode Laser with LI Curve

The plot below (Figure 31) was taken from values recorded using an optical spectrum analyser. The fluorescence portion of the graph is clearly visible until a pump current of  $\approx 23$  mA is reached. The linear segment following this is an indication that lasing is occurring. A linear regression is carried out on this segment – see Figure 32 below. The TEC was set to  $\approx 20$  °C throughout the data accumulation.

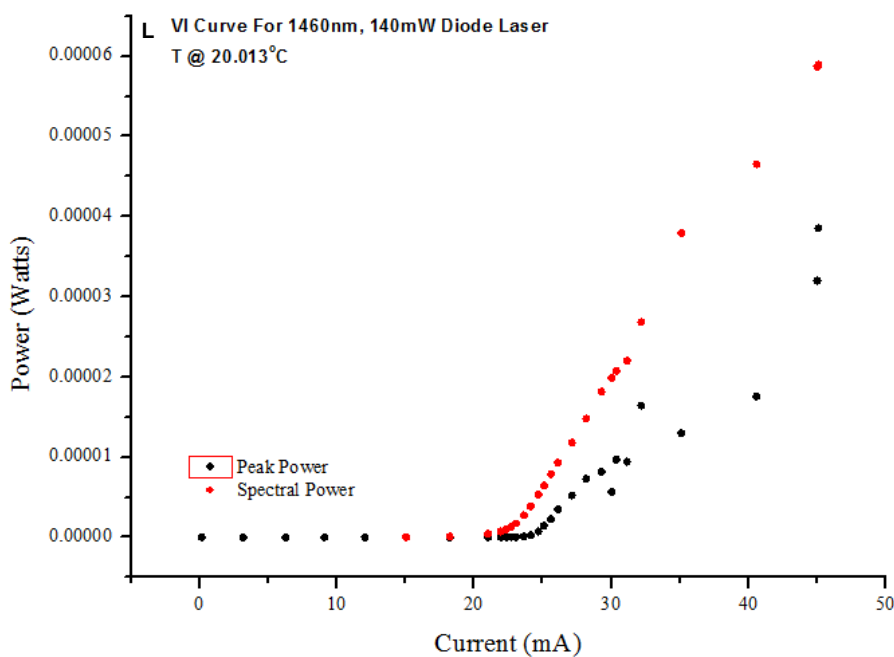


Figure 31: Power versus pump current for a diode laser using an optical spectrum analyser.

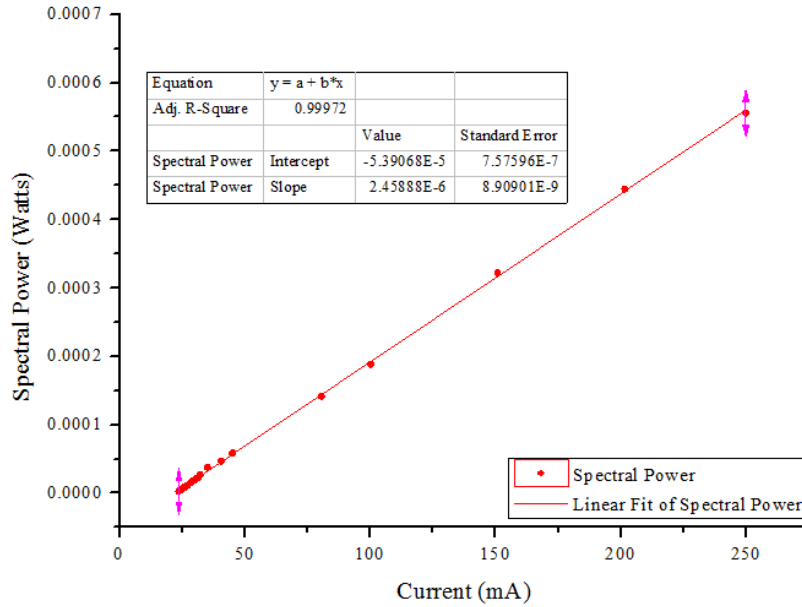
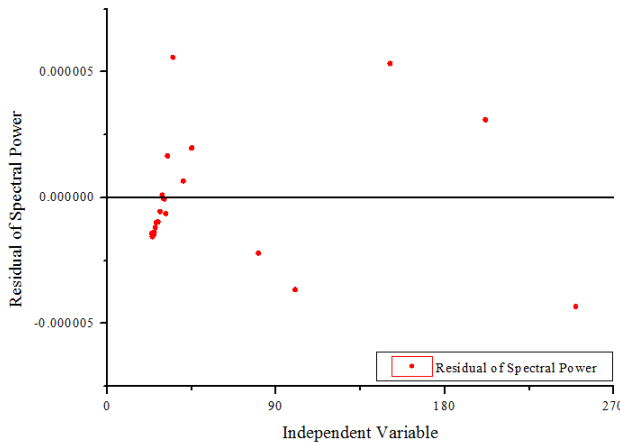


Figure 32: Linear regression applied to the lasing segment of the LI curve.

Threshold current occurs at  $x = -a/b$ :  $x = \frac{5.39068 \times 10^{-5}}{2.45888 \times 10^{-6}} = 21.92331468 \text{ mA} \approx 21.92 \text{ mA}$



A plot of the residuals shows a strong correspondence between the data and linear fit (see Figure 33 to the left).

The error in the threshold current is given by the error in  $a$  and  $b$  as follows:

$$x = \frac{a}{b} \Rightarrow \ln x = \ln a - \ln b$$

$$\frac{\Delta x}{x} = \frac{\Delta a}{a} + \frac{\Delta b}{b}$$

$$\Rightarrow \Delta x = x \left( \left| \frac{\Delta a}{a} \right| + \left| \frac{\Delta b}{b} \right| \right)$$

Figure 33: Plot of residuals from the linear regression of the second linear segment of the LI curve.

$$\Rightarrow \Delta x = (21.92) \left( \frac{7.57596 \times 10^{-7}}{5.39068 \times 10^{-5}} + \frac{8.90901 \times 10^{-9}}{2.45888 \times 10^{-6}} \right) = 0.387480053 \text{ mA} \approx 0.39 \text{ mA}$$

An LI curve was also generated using a photodiode detector (Figure 34 below). These results are less successful than those obtained using the OSA but they allow comparison of power values and an estimate of the transmission loss due to fibre connectors and dispersion through a length of fibre. Further, we see the median values for  $I_{th}$  using each method correlate strongly despite the large error term associated with the photodiode method.

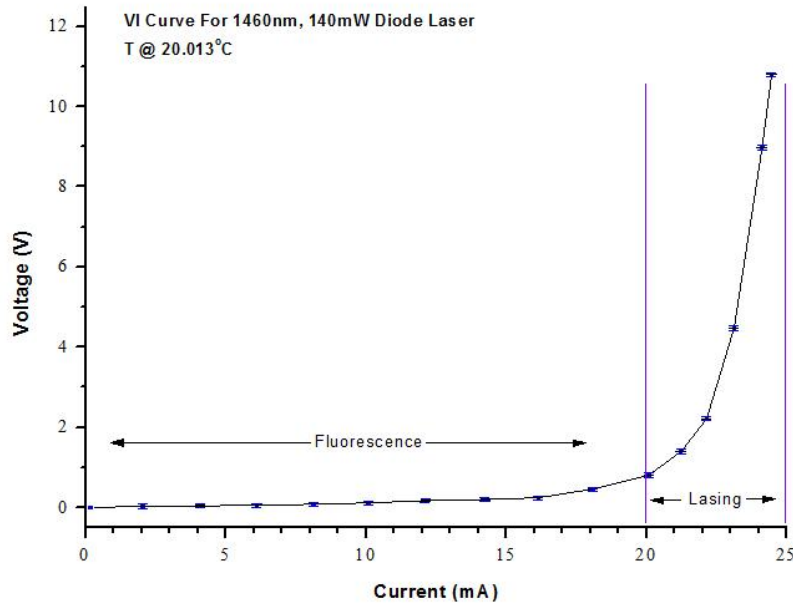


Figure 34: VI curve for diode laser using a photodiode detector.

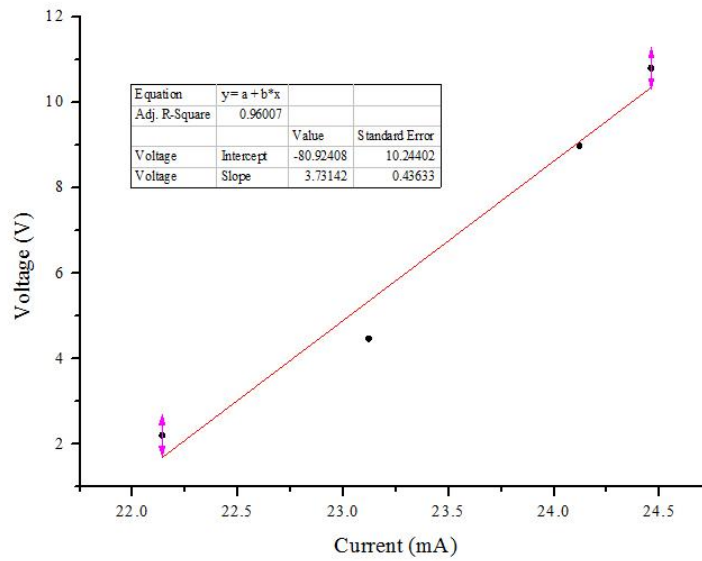


Figure 35: Linear regression applied to the lasing portion of the plot in Figure 34.

The current threshold occurs at  $V = 0$ :  $0 = -80.92408 + (3.73142)x \Rightarrow x = 21.69 \text{ mA}$ . The error in this value is due to the error in  $a$  and  $b$  according to –

$$x = \frac{a}{b} \Rightarrow \ln x = \ln a - \ln b$$

$$\frac{\Delta x}{x} = \frac{\Delta a}{a} + \frac{\Delta b}{b}$$

$$\Rightarrow \Delta x = x \left( \frac{\Delta a}{a} + \frac{\Delta b}{b} \right)$$

$$\Rightarrow \Delta x = (21.69) \left( \frac{10.24402}{80.92408} + \frac{0.43633}{3.73142} \right) = 5.28 \text{ mA}$$

This uncertainty is relatively large but reflects well the poor spread of values obtained for the linear regression. With the threshold current value in mind, the point at which we can expect lasing from the diode laser is known once we maintain a temperature of approximately 20 °C.

### 5.3.2 Optical Tweezers Set-Up 1

The initial set-up of the optical tweezers was problematic and will be discussed in further detail from page 37. In particular, issues such as the use of immersion oil, cover slips and bead-dispersion will be addressed. Nonetheless, a number of important imaging and electronic techniques were utilised during the initial set-up. A number of observations of beads undergoing Brownian motion were made and recorded using *Movie Maker*. Figures 36 below show frames from videos made while Figure 37 is a top-down view of the initial apparatus. There, the CCD camera has its front lens mounted and is aimed at the back end of the microscope objective. Figure 36 is slightly out-of-focus to display the diffraction effects observed at such high-power magnification (100×).

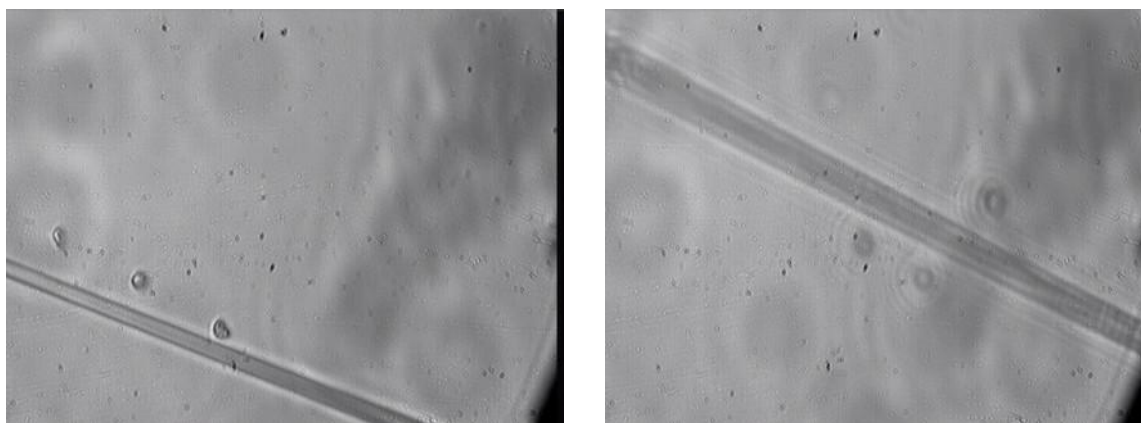


Figure 36: Beads undergoing Brownian motion and displaying diffraction effects.

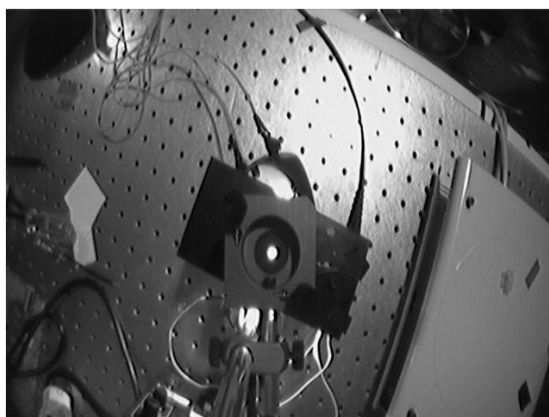


Figure 37: Top-down view of the initial apparatus.

The use of a cover slip was problematic in this set-up. The working distance of the oil immersion objective was  $\sim 0.17$  mm which is much less than the width of a glass slide. Instead, the objective was used without oil and pushed directly into the bead-water sample. This caused unnecessary movement of the suspension when the objective was focused. This was, in hindsight, one of the greatest difficulties in using the first set-up.

### 5.3.3 Optical Tweezers Set-Up 2

The second set-up was the more successful of both attempts – yielding surprising results which will be analysed in the following pages. Using a  $\sim 1$   $\mu\text{m}$  taper, a glycerol-water-bead suspension was deposited around the taper on a glass slide. The diode laser was switched on and the TEC was set to  $\approx 20$   $^{\circ}\text{C}$ . The pump current was slowly increased above  $I_{\text{th}}$  and the beads, rather than being propelled in the direction of the electric field (left to right in the following diagrams), were pushed from right to left and away from the taper. The overall motion was the opposite of that expected. The frames shown in Figure 38 were grabbed from a manual-steering video where the beads were moved by increasing and decreasing the pump current. The highlighted bead was steering in towards the taper by decreasing the pump current and steered away by increasing the current. Fibre movement is due to human interference – the lab bench on which the apparatus was used was also being used for separate experimental work simultaneously. Bead control was observed independently of fibre movement. It should also be noted that many of the “beads” appearing in Figure 38 are not actually beads – these are background dirt. This was verified by attempting, and failing, to focus on these bead-like objects.

After an intensity modulator was connected to the LDC, it was very interesting to note the range over which this bead control could be maintained. Videos were recorded of beads undergoing stable oscillations (displaying position control to *well* within  $\sim 0.5$   $\mu\text{m}$ ) up to 3 mm away from the taper – at all frequency ranges (1 Hz to 500 Hz). The penetration depth of the evanescent field when entering a water-glycerol solution should be no more than 0.5  $\mu\text{m}$ .

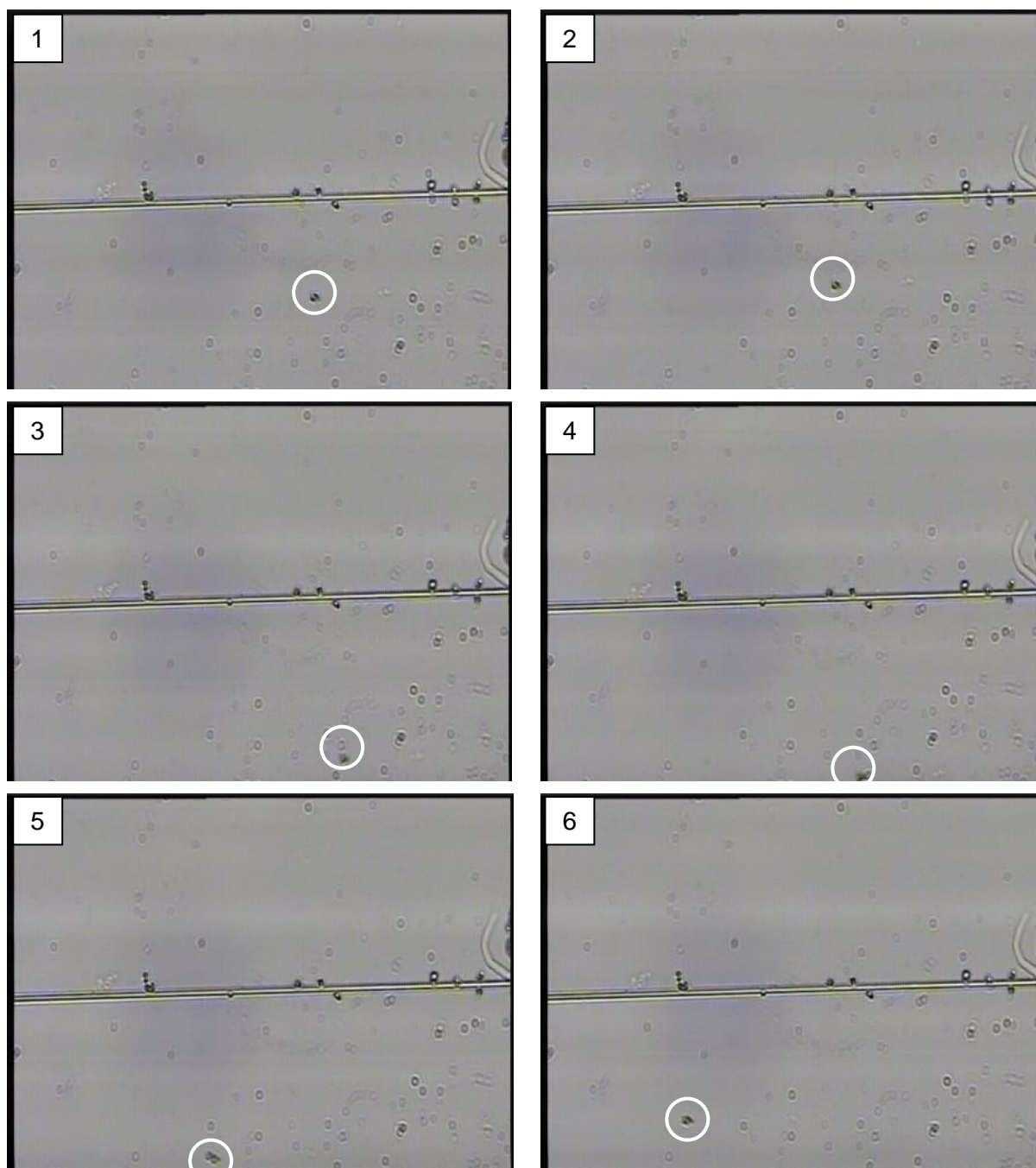


Figure 38: Successive frames from a video showing manual steering of the beads.

Using the captured videos, properties of the bead movements could be analysed. With the intensity modulator, oscillations of the beads were recorded. A plot of velocity versus frequency was generated for various sample beads. A linear relationship between speed and frequency is evident as well as a reciprocal relationship between the period of oscillation of the beads and their frequencies. This is as expected when considering any particle undergoing forced harmonic oscillation.

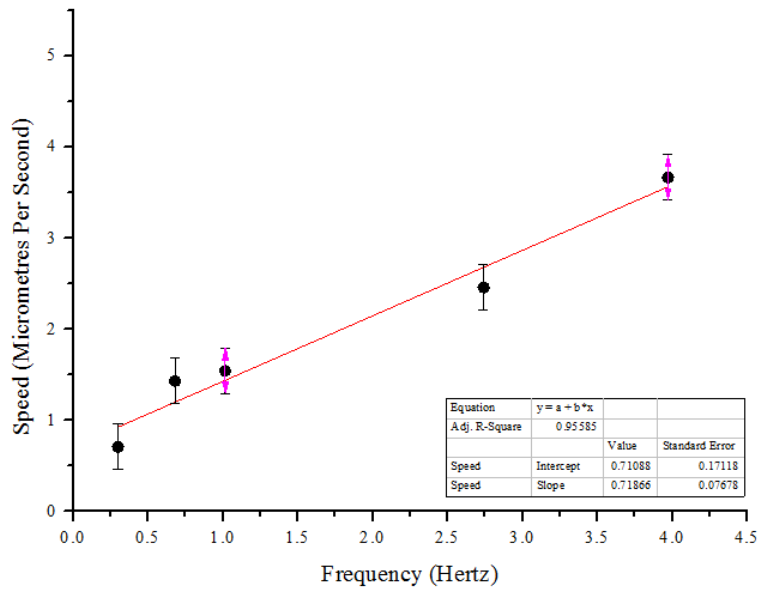


Figure 39: Speed versus frequency for a particular sample of beads undergoing forced harmonic motion.

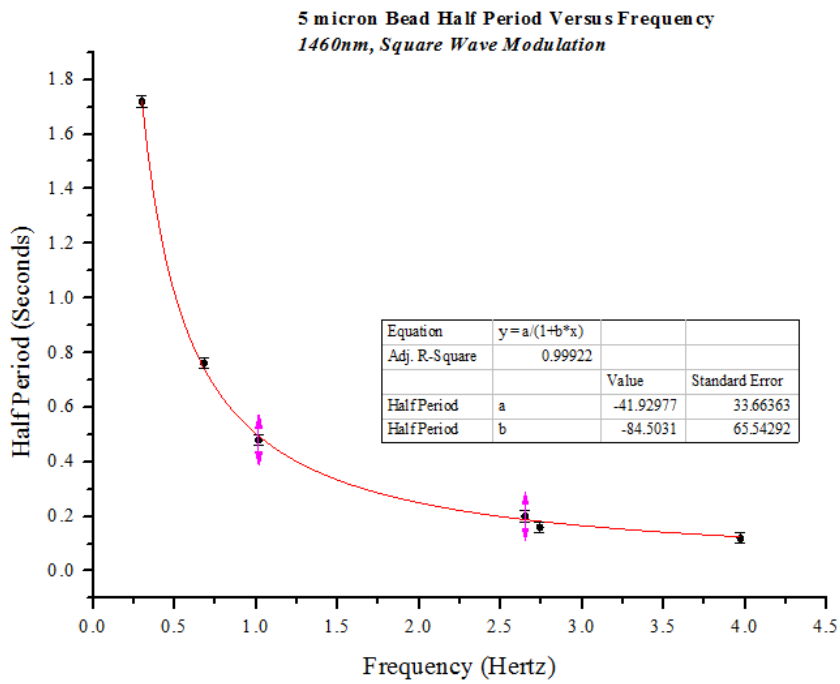
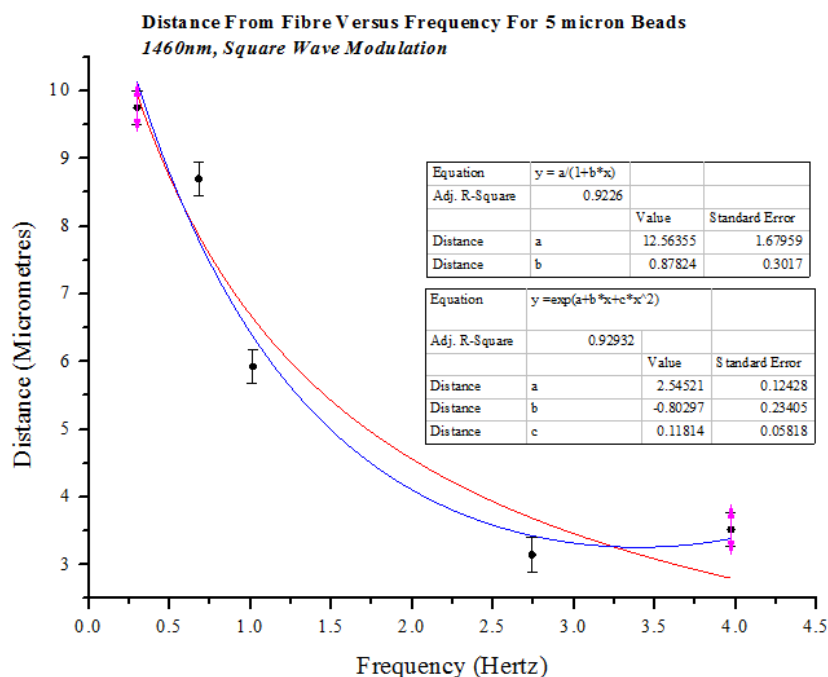


Figure 40: Period as a function of frequency for a sample of beads undergoing forced harmonic motion.

Plotting distances between certain beads and the taper as a function of oscillation frequency, we see interesting behaviour (Figure 41 below). Both a reciprocal plot (red) and exponential plot (blue) were applied to the data points and their modest uncertainties values. It is most likely that the reciprocal behaviour is behind the movement of the beads rather than the exponential behaviour.



**Figure 41: Distance from taper to bead as a function of frequency.**

One of the main difficulties during the image analysis of this experiment was the final frame rate in Movie Maker. A frame was taken every 4 ms which put a definite upper limit to the analysis on high frequencies of oscillation. The high frequency beads appeared as a blur on screen rather than an independent bead movement across the successive frames.

During intensity modulation, a worrying observation was taper movement – not purely due to human interference with the optical bench on which the apparatus was set up, but periodic movement which seemed to correlate with the bead movement. This taper movement seemed only to occur during modulation of the field. Later, it was found that the taper was “loose” due to a scuff off the side of the glass slide above which it was mounted. Although it was desirable to have the taper and glass slide parallel, it was difficult to adjust the slide so that it was parallel to the fibre. Most likely, during the experiment, the slide was accidentally moved and scuffed the fibre cladding, loosening the taper between its mounts.

After observing this highly long-range force which allowed bead control up to 3 mm from the taper, a different diode laser, with  $\lambda = 980$  nm and approximately the same power output, was used. This particular wavelength was advantageous as the CCD camera in use was sensitive to this light – the light field from the taper could be observed visually. To eliminate the possibility of enhanced polarity effects in water, glycerol was not used during this second run – a solution of water only was used to suspend the polystyrene beads. The same results were observed and in a more stable manner as no correlated taper movements were found.

Another striking feature of this long-range control was observed when enormous clumps of beads could be moved easily with appropriate pump current. Even under field modulation, it was regularly observed that clumps of 50 beads were undergoing stable oscillations. Some images of these are shown below in Figure 42.

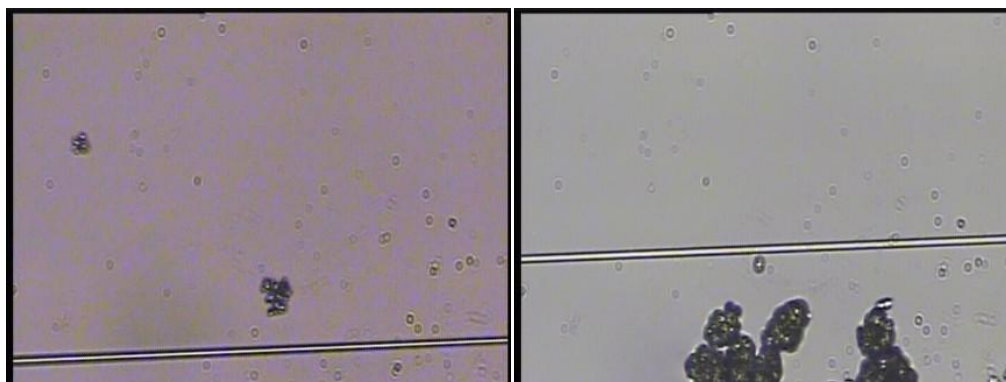
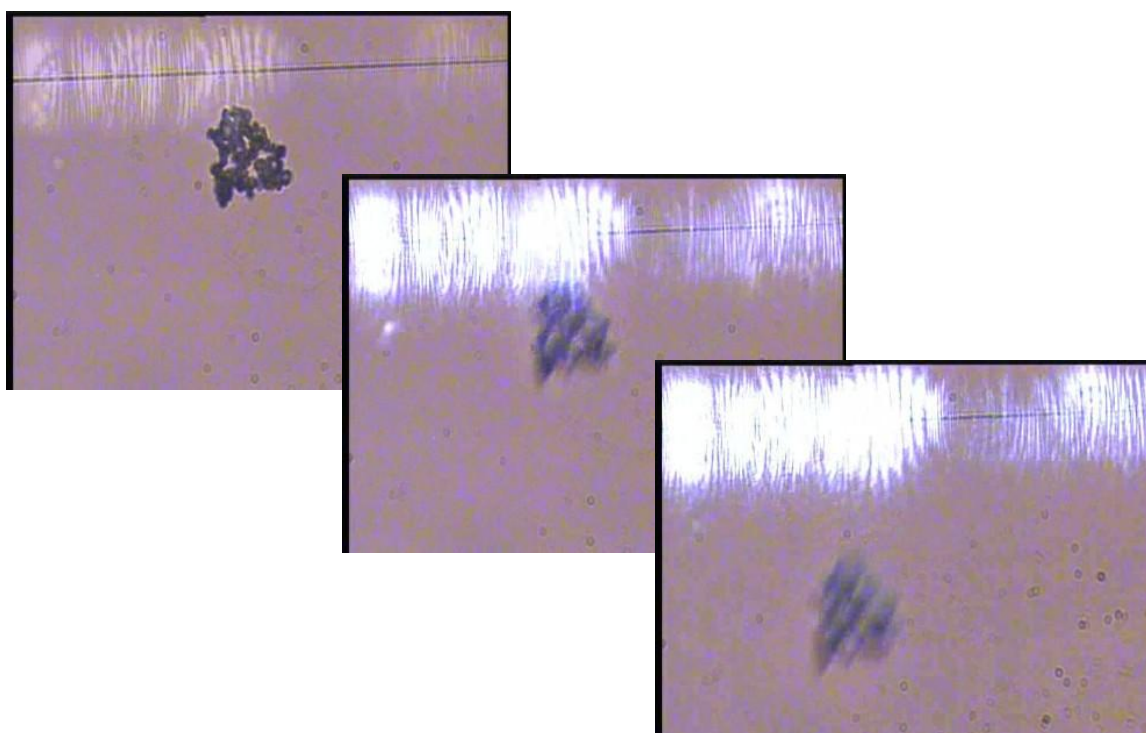


Figure 42: (Above and below) Movement of very large clumps of beads was observed even with modest laser power.



In the last image array above, we see the electric field switching on and the resulting bead movement over approximately 50  $\mu\text{m}$ .

Bead clumping was initially to be a problem but because such large groups of beads could be propelled, the clumping issue was not rectified. In theory, clumping can be dealt with by using a mixing agent such as *PBS* (phosphate buffered saline). This salty buffer helps maintain a constant pH. By adding the *anti-coagulant* EDTA to PBS, the beads de-clump.



Figure 43: Polyamide seeding particles (PSP) used in the trapping experiment.

There is a large possibility that the non-uniform shapes of the beads contributed to the failure to trap them (see Figure 43). In trapping theory, spherical shapes are assumed and it is intuitive to consider that non-spherical particles give rise to *rotations*. In fact, in Figure 42 above, immediately after these three frames, the large non-uniform clump of beads undergoes rotations at the bottom of the screen while the electric field remains constant for a certain length of time. This is shown below in Figure 44.

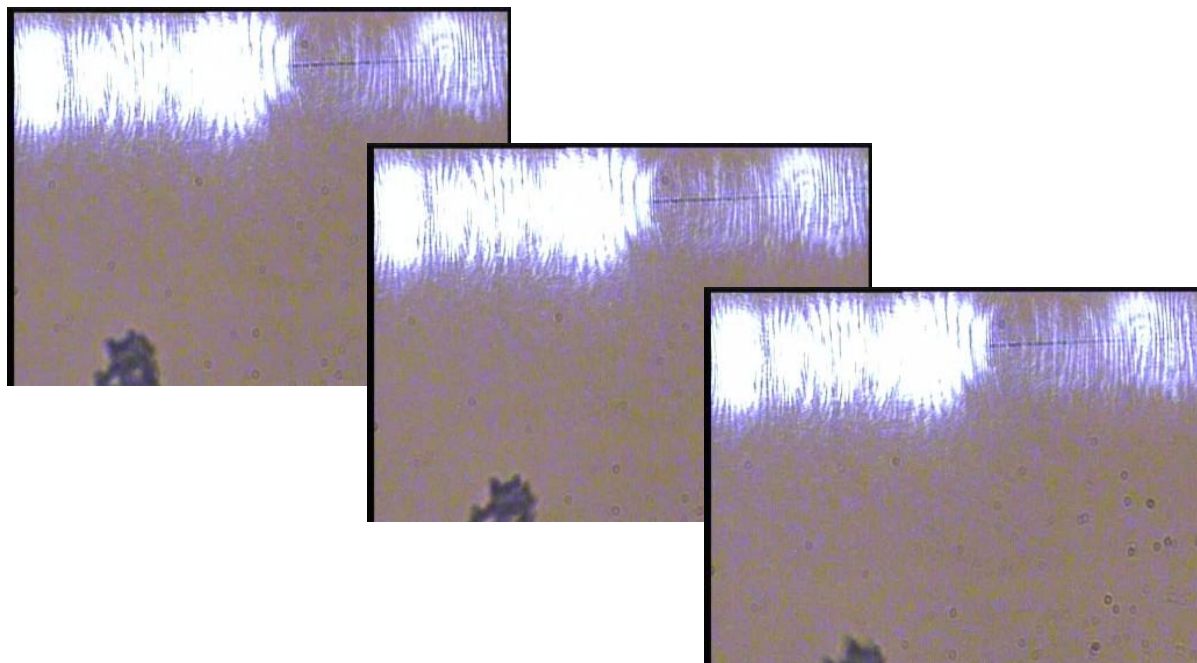


Figure 44: Rotation of non-uniform bead clumps.

### 5.3.4 Water Absorption

The H<sub>2</sub>O molecule absorbs over a very large range of wavelengths as it possess many vibrational states. The amplitudes of these vibrations are large because the hydrogen atom is relatively light. Considering the case where light is incident on a water molecule: If a vibration brings a change in dipole moment in the molecule, a photon of the appropriate frequency will be absorbed. It is noted that the water molecule exhibits strong absorption around  $\lambda = 1450$  nm and 970 nm (Carter & McCain, 1993) (Rossel & McBratney, 1998) (Jacquemoud & Ustin, 2003) – very close to the wavelengths of light used in this trapping experiment. A possible explanation for this long-range bead control could be water absorption effects. In particular, dealing with non-uniform PSPs, static affects could be induced due to changing dipole moments in the already polar water molecule. One strong way in which this concept could be explored is by repeating the optical trapping experiment using a laser wavelength in the low visible spectrum. If it is indeed H<sub>2</sub>O absorption at work, we should observe a large reduction in the bead-control effect.

## 5.4 CONCLUSION

This project investigated the lower limit of laser power need to perform optical trapping using polyamide seeding particles of diameter  $\sim 5 \mu\text{m}$ . Throughout the project, skills in electronics (soldering, circuit-building) and optical fibre handling (cleaving, splicing) were gained. During the second attempt at optical trapping, an unusual ‘anti-trapping’ force was observed which pushed the beads far from a  $1 \mu\text{m}$  taper in a direction opposite to that expected (i.e. opposite to the direction of the electromagnetic field). When the light field was modulated using various waveforms, the beads exhibited stable oscillations up to 3 mm from the taper. Possible explanations for this long-range force include water absorption effects, static charge accumulation due to  $\text{H}_2\text{O}$  polarity and non-spherical trapping particle effects.

In general, further improvements in terms of trapping power can be made by using a higher power laser. A 300 mW CW should, in theory, supply adequate power to trap these particles. In the absence of a high-power laser, an extra voltage can be applied to the taper by connecting either end to a power supply. Appropriate resistors would have to be used at the laser end to avoid combustion of the fibre.

Finally, the use of spherical rather than “round” beads could be used in future experiments. This would qualify assumptions that the trapping particles exhibit equal radiation pressure forces in all directions (spherical symmetry).

## 6. ACKNOWLEDGEMENTS

Unfortunately, it is the nature of experimental research that gives strength to Murphy's Law – you cannot always obtain results, or, if you do, they're not exactly as expected. Nevertheless, the experience and knowledge that I have gained over the past term far outweighs any disappointment I may have over not observing what I expected to observe. I would like to thank the Quantum Optics Group for their help and support throughout the project. Particularly, Dr. Síle Nic Chormaic for her guidance, Jonathan Ward for his "troubleshooting" towards the end, Michael Morrissey and Kieran Deasy for their masterminded electronics and Prof. Vladimir Minogin for his expert opinions. I would also like to thank Prof. Paul Brint for helping me acquire various odds and ends from the Chemistry Department in UCC.

## 7. REFERENCES

- [1] A. Ashkin, J.M. Dziedzic, J.E. Bjorkholm and S. Chu. 1986. "Observation of a Single-Beam Gradient Force Optical Trap for Dielectric Particles." *Opt. Lett.* 11 (5) 288-290.
- [2] Samori bruno; zuccheri g.; baschieri p.; *Protein unfolding and refolding under force: Methodologies for nanomechanics*, *ChemPhysChem* (2005), vol. 6, no. 1, pp. 29-34
- [3] Ibrahim Bukusoglu, Cagatay Basdogan, Alper Kiraz, Adnan Kurt, *Haptic Manipulation of Microspheres Using Optical Tweezers*, *Proceedings of the Symposium on Haptic Interfaces for Virtual Environment and Teleoperator Systems* (2006)
- [4] V. Sandoghdar, F. Treussart, J. Hare, V. Lefèvre-Seguin, J. -M. Raimond, and S. Haroche, *Very low threshold whispering-gallery-mode microsphere laser*, *Phys. Rev.* (1996), A 54, R1777 - R1780
- [5] G Brambilla, G Senthil Murugan, J S Wilkinson, D J Richardson, *Optical manipulation of microspheres along a subwavelength optical wire*, *Opt Lett.* (2007) Oct 15; 32, (20):3041-3
- [6] Eugene Hecht, *Optics* (4<sup>th</sup> ed.), Addison Wesley (2002), Page 586
- [7] Javan, Ali; Bennett Jr., William; Herriott, Donald, *Population Inversion and Continuous Optical Maser Oscillation in a Gas Discharge Containing a He-Ne Mixture*, *Physical Review Letters* (1961), 106-110
- [8] Eoin O'Reilly, *Quantum Theory of Solids* (1<sup>st</sup> ed.), CRC (October 24, 2002), Page 99, Eqn 5.4
- [9] Dan Monroe, *The Optical Trap*, *The Scientist* (2005), Vol 19, Issue 16, Page 48
- [10] James R. Webb, Ulf L. Österberg, *Optoelectronics for Data Communication*, Academic Press (1995), Chapter 2, Page 7
- [11] Quincke G. (1866a): "Optische Experimental-Untersuchungen. I Über das Eindringen des total reflektierten Lichtes in das dünnere Medium", *Ann. Phys.*; 127, 1
- Quincke G. (1866ba): "Optische Experimental-Untersuchungen. II. Über die elliptische Plarisation des bei totaler Reflexion eingedrungenen oder zurück-geworfenen Lichtes", *Ann. Phys.*; 127, 199
  - Hall E. E. (1902): "The penetration of totally internally reflected light into the rare medium", *Phys. Rev.*, 15, 73
  - Bose J. C. (1897): "On the influence of the thickness of air-space on total reflection of electric radiation", *Proc. R. Soc. London*, 62, 300
- [12] Ajoy Kumar Ghatak, K. Thyagarajan , *Optical Electronics*, Cambridge University Press (1989), Eqn 2.59
- [13] F. De Fornel, *Evanescent Waves From Newtonian Optics to Atomic Optics*, Springer (1997), Page 12.
- [14] F. Goos and H. Hänchen, *Ein neuer und fundamentaler versuch zur totalreflexion*, *Ann. Phys.* (1947) 1, 333-346
- [15] S. M. Spillane, T. J. Kippenberg, O. J. Painter, and K. J. Vahala, *Phys. Lett. Rev.* **91**, 043902 (2003).
- [16] T. E. Dimmick, G. Kakarantzas, T. A. Birks, and P. St. J. Russel, *Appl. Opt.* **38**, 6845 (1999).
- [17] M. Sumetsky, Y. Dulashko, J. M. Fini, A. Hale, and D. J. DiGiovanni, *J. Lightwave Technol.* **24**, 242 (2006).

[18] Ward, J. M., O'Shea, D. G., Shortt, B. J., et al, *Heat-and-pull ring for taper fabrication*, Rev. Sci. Ins. **77**, 083105 (2006)

[19] Mark C. Williams, *Optical Tweezers: Measuring Piconewton Forces*, Previously published in Biophysics Textbook Online

[20] Neuman, Keir C.; Block, Steve M., *Optical Trapping*, Rev. Sci. Instrum. 2787-2809 (2004)

[21] D. C. Weber and E. D. Hirleman, *Light scattering signatures of individual spheres on optically smooth conducting surfaces*, Appl. Opt. **27**, 4019- (1988)

[22] Eugene Hecht, *Optics* (4<sup>th</sup> ed.), Addison Wesley (2002), Page 599

## 8. APPENDIX A – SPECIFICATION SHEET

### 8.1 USB Spectrometer

Physical	
Dimensions:	89.1 mm x 63.3 mm x 34.4 mm
Weight:	190 grams
Detector Specifications	
Detector:	Toshiba TCD1304AP Linear CCD array
Detector range:	200-1100 nm
Pixels:	3648 pixels
Pixel size:	8 $\mu\text{m}$ x 200 $\mu\text{m}$
Pixel well depth:	100,000 electrons
Signal-to-noise ratio:	300:1 (at full signal)
A/D resolution:	16 bit
Dark noise:	50 RMS counts
Corrected linearity:	>99.8%
Sensitivity:	130 photons/count at 400 nm; 60 photons/count at 600 nm
Electronics	
Power consumption:	250 mA @ 5 VDC
Data transfer speed:	Full spectrum to memory every 5 ms with USB 2.0 port
Inputs/Outputs:	Yes, 8 onboard digital user-programmable GPIOs
Analog channels:	No
Auto nulling:	Yes
Breakout box compatible:	Yes, HR4-BREAKOUT
Trigger modes:	4 modes
Strobe functions:	Yes
Connector:	22-pin connector
Computer	
Operating systems:	Windows 98/Me/2000/XP, Mac OS X and Linux with USB port; Any 32-bit Windows OS with serial port
Computer interfaces:	USB 2.0 @ 480 Mbps (USB1.1 compatible); RS-232 (2-wire) @ 115.2 K baud
Peripheral interfaces:	SPI (3-wire); I2C inter-integrated circuit

Optical Bench	
Design:	f/4, Asymmetrical crossed Czerny-Turner
Focal length:	42 mm input; 68 mm output
Entrance aperture:	5, 10, 25, 50, 100 or 200 $\mu\text{m}$ wide slits or fiber (no slit)
Grating options:	14 different grating options, UV through Shortwave NIR
HC-1 grating option:	No
Detector collection lens option:	Yes, L4
DET4 filter options:	DET4-200-850; DET4-350-1000
Other bench filter options:	Longpass OF-1 filters
Collimating and focusing mirrors:	Standard or SAG+UPG
UV enhanced window:	Yes, UV4
Fiber optic connector:	SMA 905 to 0.22 numerical aperture single-strand optical fiber
Spectroscopic	
Wavelength range:	Grating dependent
Optical resolution:	$\sim$ 0.3-10.0 nm FWHM (grating dependent)
Signal-to-noise ratio:	300:1 (at full signal)
A/D resolution:	16 bit
Dark noise:	50 RMS counts
Integration time:	3.8 milliseconds to 10 seconds
Dynamic range:	$2 \times 10^8$ (system), 1300:1 for a single acquisition
Stray light:	<0.05% at 600 nm; 0.10% at 435 nm

## 8.2 Diode Laser

## Data Sheet

FOL1402Pxy / 1480nm Pump Laser Module

ODC-2A001D Date Jan.09.2003

## Absolute Maximum Ratings

Parameters	Sym.	Min.	Max.	Unit	Parameters	Sym.	Min.	Max.	Unit
Storage Temperature	Tstg	-40	85	°C	PD Forward Current	IfPD	-	5	mA
Operating Case Temperature	Tc	-20	75 <sup>1)</sup>	°C	PD Reverse Voltage	VrPD	-	20	V
LD Forward Current	If	-	1000	mA	TEC Current	Ic	-0.6	2	A
LD Reverse Voltage	Vr	-	2	V	TEC Voltage	Vc	-	4.5	V

1) FOL1402PN series: Max. 70°C

## Optical and Electrical Specifications (Sensor Temperature (Ts) = 25°C)

Parameters	Sym.	Min.	Typ.	Max.	Unit	Conditions
Output Power	Pf <sup>2)</sup>				mW	
FOL1402PJX		120	-	-		IfBOL=<500mA, max. ΔT=50°C
FOL1402PJY		130	-	-		
FOL1402PLZ		140	-	-		IfBOL=<600mA, max. ΔT=50°C
FOL1402PLE		150	-	-		
FOL1402PLF		160	-	-		
FOL1402PMG		170	-	-		IfBOL=<700mA, max. ΔT=50°C
FOL1402PMH		180	-	-		
FOL1402PMI		190	-	-		
FOL1402PNJ		200	-	-		IfBOL=<800mA max. ΔT=45°C
Center Wavelength(FP)	$\lambda_c$	1460	-	1490	nm	RMS(-20dB), Rated Power
Center Wavelength(FBG)	$\lambda_c^{3)}$	$\lambda_c-1.5$	$\lambda_c$	$\lambda_c+1.5$	nm	RMS(-20dB), Rated Power
Spectral Width(FP)	$\Delta\lambda$	-	-	8	nm	RMS(-20dB), Rated Power
Spectral Width(FBG)	$\Delta\lambda$	-	-	3	nm	RMS(-20dB), Rated Power
LD Operating Forward Voltage	Vf	-	-	2.5	V	Rated Power
LD Forward Current at EOL	IfEOL	-	-	1.2xIfBOL	mA	End of Life
Monitor Current	Im	50	-	1000	μA	VrPD=5V, Rated Power
Monitor Dark Current	Id	-	-	100	nA	VrPD=5V
Extinction Ratio	Re	16	-	-	dB	Type4 and Type6
Isolation	Iso	30	-	-	dB	Type3 and Type4
TEC Spec.	-	Refer to below			-	-
Thermistor Resistance	Rth	9.5	10	10.5	kΩ	Ts=25°C
Thermistor B Constant	Bth	-	3900	-	K	Ts=25°C

2)Pf: Available Pf may depend upon center wavelength selected.

3) $\lambda_c$ : Selected center wavelength from 1380nm to 1520nm available.

## Thermo-Electric Cooler Characteristic &amp; Power Consumption

Condition	Max Val., Ts=25°C, ΔT=45°C, IfEOL			Max Val., Ts=25°C, ΔT=50°C, IfEOL		
	Itec[A]	Vtec[V]	4)Ptotal[W]	Itec[A]	Vtec[V]	4)Ptotal[W]
PJ* series Pf=120 to 130[mW]	1.1	2.4	3.5	1.2	2.7	4.0
PL* series Pf=140 to 160[mW]	1.2	2.7	4.4	1.3	3.0	5.1
PM* series Pf=170 to 190[mW]	1.4	3.1	5.8	1.5	3.5	6.8
PN* series Pf=200[mW]	1.7	3.6	7.8	-	-	-

4) Ptotal = Wtec + Wld (Total Power Consumption)